

Parametric frequency conversion in two coupled superconducting resonators

Master's thesis in Nanotechnology

ANDREAS BENGTSSON

MASTER'S THESIS 2015:05

Parametric frequency conversion in two coupled superconducting resonators

ANDREAS BENGTSSON



CHALMERS
UNIVERSITY OF TECHNOLOGY

Department of Microtechnology and Nanoscience
Quantum Device Physics Laboratory
Experimental Mesoscopic Physics
CHALMERS UNIVERSITY OF TECHNOLOGY
Gothenburg, Sweden 2015

Parametric frequency conversion in two coupled superconducting resonators
ANDREAS BENGTTSSON

© ANDREAS BENGTTSSON, 2015.

Supervisor and examiner:
Jonas Bylander

Master's Thesis 2015:05
Department of Microtechnology and Nanoscience
Quantum Device Physics Laboratory
Experimental Mesoscopic Physics
Chalmers University of Technology
SE-412 96 Gothenburg
Telephone +46 31 772 1000

Cover: Micrograph of the two coupled superconducting resonators used in this project.

Typeset in L^AT_EX
Printed by Reproservice
Gothenburg, Sweden 2015

Parametric frequency conversion in two coupled superconducting resonators
ANDREAS BENGTSSON
Department of Microtechnology and Nanoscience
Chalmers University of Technology

Abstract

In this work, we have designed, fabricated, and characterized two coupled superconducting microwave resonators.

Using this system, we investigate a parametric frequency conversion process in the microwave regime. We modulate the resonance frequency at the difference frequency between two modes, i.e. by three-wave mixing. An incoming signal, resonant with one of the modes, is then converted to the other mode. We demonstrate this behavior in several different schemes, e.g. using one or two modulation tones. We report a conversion efficiency of 50%, meaning that 50% of the incoming wave amplitude gets converted to the other frequency.

Finally, we discuss the possibilities to use such a system in a quantum computing architecture.

Keywords: Frequency conversion, Parametric, Superconducting, Coupled, Resonators, Microwave, Beam splitting.

Acknowledgements

First of all, a big thank you to my supervisor Jonas Bylander for your great support and leadership. This thesis wouldn't exist without your guidance, attention to details and proof reading. Second I wish to express my gratitude to Philip Krantz who took me under his wings and taught me everything he knows, all from fabrication to sailing knots. I thank Arsalan Pourkabirian and Michaël Simoen for letting me borrow your office and answering all my questions about measurement techniques, qubits and cryogenics. Two people that helped me and this project a lot is professor Per Delsing and professor Vitaly Shumeiko, thank you for all your support with theory, without that I wouldn't have made it. I also would like to thank Sumedh Mahasahbde for introducing me to the field of nanoscience and all your help and ideas in the clean room.

Last, a big thank you to all the other people at QDP for making it a great place to work in, especially Niclas Lindvall, Maria Ekström, David Niepce, Ida-Maria Svensson, Thomas Aref, Seckin Kintas and Ben Schneider.

Andreas Bengtsson, Gothenburg, May 2015

Contents

List of Figures	x
List of Tables	xiii
1 Introduction	1
1.1 Quantum physics	1
1.1.1 Quantum optics	2
1.1.2 Quantum computing	3
1.2 Goals of this project	4
2 Theoretical descriptions	5
2.1 Superconductivity	5
2.1.1 The Josephson effect	6
2.1.2 SQUID	6
2.2 Transmission lines and resonators	7
2.2.1 Resonators	7
2.2.2 Co-planar waveguides	9
2.2.3 Tunable resonators	10
2.2.4 Two coupled resonators	11
2.3 Parametric pumping	13
2.3.1 Frequency conversion	13
3 Experimental methods	17
3.1 Simulations and device modeling	18
3.2 Fabrication	19
3.3 Cryogenics and measurements	21
3.3.1 Measurement setup	21
3.3.2 Measurement techniques	22
4 Results and discussion	27
4.1 Initial characterization	27
4.1.1 Crosstalk - DC and RF	30
4.2 Frequency conversion	31
4.2.1 Degenerate case	31
4.2.2 Non-degenerate case	35
5 Conclusions and outlooks	39

CONTENTS

Bibliography	41
A Clean room processes	I
B Derivation of the Josephson-relations	III
C Derivation of the superconducting phase in two coupled resonators	V

List of Figures

1.1	Illustration of the principle behind two optical devices. a) Beam splitter, one input that is split into two outputs. The color of the light is preserved b) Frequency converter, one input and one output, but the light is split into two different colors.	3
2.1	Illustration of a SQUID. It consists of two Josephson junctions (represented as squares with a cross) in parallel, effectively forming a loop. Φ denotes the magnetic flux through this loop.	7
2.2	An electrical resonator coupled to a transmission line. The resonance frequency is given by $\omega_r = 1/\sqrt{L_R C_R}$. R_R describes the losses inside the resonator.	8
2.3	A schematic of the co-planar waveguide. w is the width of the center conductor and g is the gap between the center conductor and the ground planes.	9
2.4	$\lambda/4$ resonator based on a CPW. a) Illustration of the resonator. At the top is the coupling capacitor, and at the bottom the center conductor is shorted to the ground planes. Not to scale, d is usually orders of magnitude larger than both the width of the center conductor and the width of the gaps. b) Electric potential as a function of the position inside a $\lambda/4$ resonator. c) Equivalent circuit close to resonance.	10
2.5	Equivalent electrical circuit for two coupled $\lambda/4$ resonators each terminated by a SQUID, close to resonance. 1 and 2 denotes the reference ports used in the ABCD-matrix calculation.	12
2.6	Mode structures for two identical, coupled, $\lambda/4$ cavities, each terminated by a SQUID, c.f. Figure 2.5. Plotted is the superconducting phase, as a function of position inside the resonators, in units of d , the length of one resonator. The coupling capacitor C_c is located at $x = 0$	13
2.7	Matrix elements for frequency conversion. (a) Zero and finite internal loss. Blue lines are for $\Gamma_i^{(1)} = \Gamma_i^{(2)} = 0$, while red represents a finite internal loss $\Gamma_i^{(1)} = \Gamma_i^{(2)} = 0.2\Gamma_0^{(1)}$. Solid lines are $ V_{11} $ and dotted lines $ V_{12} $. For all traces $\epsilon = 10\Gamma_0^{(1)} = 10\Gamma_0^{(2)}$. b) Frequency conversion efficiency, $\max(V_{12})$, as a function of the ratio between internal and external loss, assuming identical resonators.	16

3.1	Illustration of a co-planar waveguide (CPW). In this work the substrate is made of sapphire (Al_2O_3), with a relative dielectric constant $\epsilon_r = 9.3$. The metal is niobium, and the center conductor width $w = 15 \mu\text{m}$, and a gap width $g = 6 \mu\text{m}$. Above the CPW is only vacuum, with the relative dielectric constant 1.	18
3.2	Micrographs of the fabricated sample used in this project. (a) Two capacitively coupled $\lambda/4$ resonators, each terminated by a SQUID, with their flux lines for DC-tuning and RF-pumping, and their transmission lines for probing. Along the edges are six test structures, each containing one SQUID. The reason of the horizontal gap in the middle of the sample is to confine DC currents through the flux lines to their respective resonator. (b) A closer look on the SQUID and the pump line design. (c) The three capacitors used: the small one is the coupling between the two resonators and the slightly larger ones are the couplings between each resonator and the transmission lines.	20
3.3	Measurement setup used in this project. In this work we refer to the resonator, SQUID and pump line on the left side as (A) and on the other side as (B). The sample is mounted on a PCB inside a gold-plated copper box with four SMK-connectors, two for the input-output ports, and two for the flux lines. On each of the two connectors for the flux lines, a bias-tee is mounted, combining one RF and one DC line.	23
3.4	Photographs of the sample box, mounted on the tail of the mixing chamber in the dilution refrigerator. a) The sample box, together with the external coil, the two bias tees and four coaxial cables. b) The open sample box. Inside is a PCB with six CPWs, leading to the wire bonded sample with two coupled resonators.	24
3.5	The heterodyne detection scheme used in some of the characterizations of the device under test (DUT). Here we use an LO frequency 187.5 MHz above the measurement frequency f_m . Note that we can set f_s and f_m independently of each other.	25
4.1	A simplified measurement setup, showing the different signal ports, which are referred to throughout this chapter.	28
4.2	Measurements of $ S_{AA} $ as a function of global and local magnetic fluxes, together with theoretical fits. (a) Tuning of both SQUIDs with a global magnetic flux through the external coil, with zero flux offset between (A) and (B). Since there is no flux offset between the two SQUIDs, the distance between the two resonances equals $2J = 46$ MHz. (b) Tuning using flux line (B). Note the avoided crossings and also the small crosstalk to the other SQUID. (c) and (d) Extracted resonance frequencies (blue) from the data in a and b , together with theoretical fits (red) using equations (2.12) and (2.13). Plotted in d is also the predicted frequency of resonator (B) even though we cannot measure it directly.	29

4.3	<p>Pump scheme used for measuring frequency conversion. (a) The two eigenmodes of the system in the absence of a parametric pump. (b) By turning on a pump at the difference frequency, the modes couple together and hybridize into four new modes. By applying a signal B_2 close to f_2 we can measure what gets reflected, given by $V_{22}B_2$, and what gets converted, $V_{12}B_2$. The two matrix elements are given by equations (2.37) and (2.39), respectively.</p>	32
4.4	<p>Beam splitting in the degenerate case, using one pump tone on SQUID A. (a) Depicted is the measurement of S_{AA}, as a function of pump frequency f_p, at a power of $P_p = -8$ dBm at the generator. The white, dashed, lines, illustrates the invisible mode that couples to the original modes, hence creating the avoided crossings. (b) Pump amplitude dependence of the splitting distance between the two new modes, using a parametric pump at $f_p = f_1 - f_2$. The observed splitting is clearly linearly dependent on the pump amplitude, as expected from theory.</p>	33
4.5	<p>Frequency conversion using one parametric pump in two degenerate $\lambda/4$ resonators. (a) Reflected magnitude S_{AA} as a function of signal and measurement frequencies. Away from resonance, all of the applied signal is reflected back at the signal frequency, but on resonance some parts gets reflected at $f_s \pm f_p$, illustrated by the white arrows. (b) Three linecuts of a, indicated by arrows in corresponding colors. The four pairs of resonance are measurements of the magnitude of the four input-output matrix elements in equations (2.37)-(2.40), and the solid lines are fits using these equations. Blue is V_{11} and V_{22}, while green is V_{12}, and red is V_{21}. The black arrows corresponds to how the signals are converted.</p>	34
4.6	<p>Beam splitting using two degenerate pump tones, sweeping the phase offset between the two pump signals. Note that zero phase difference is set arbitrarily and has no physical meaning. (a) Experimental data, the two pump tones are set to identical frequencies $f_p = 45$ MHz and pump powers $P_p = -1$ dBm at the generators. (b) Fit of the peak separation as a function of the phase difference θ where blue is the data and red the fit with $\epsilon' = 12.5$ MHz.</p>	35
4.7	<p>Beam splitting using two pump tones. The pump on SQUID (A) is locked at 46 MHz and a power of 6 dBm at the generator, whereas the pump on SQUID (B) is swept in frequency, while maintaining a power of 2 dBm at the generator.</p>	36
4.8	<p>Beam splitting in the non-degenerate case. In both figures we measure S_{AA} as a function of pump frequency and with a constant pump power $P_p = 6$ dBm at the generator. (a) Here the pump signal is applied at SQUID (A) and for (b) it is applied at SQUID (B).</p>	37
C.1	<p>Two coupled $\lambda/4$ resonators each terminated by a SQUID.</p>	VI

LIST OF FIGURES

List of Tables

3.1	Input (to the left) and output (to the right) parameters of the conformal mapping method [1], used to simulate a co-planar waveguide. . .	18
4.1	Extracted parameters relevant to flux tuning for each of the resonators. The parameters were extracted through data fitting using equations (C.1) and (2.12). The data and the fits are shown in Figure 4.2.	30
4.2	Extracted circuit parameters for resonator (A). The uncertainty for resonator (B) was too large to be able to extract any parameters. . . .	30

LIST OF TABLES

1

Introduction

PHYSICISTS are driven by curiosity, curiosity about how the universe (or parts of it) works and how it can be described by a mathematical model. But it does not stop there: the next question is, what can we predict from these models and what happens if we do this or that? The original idea behind the work presented in this thesis arose from just a question like that. We have an idea of creating and manipulating coupled photonic condensates, but to reach that goal, we need to start somewhere.

This thesis is just that start – we present the design and fabrication of a first prototype. We carried out initial characterizations, and we also used the device to perform parametric frequency conversion, which is explained more later.

First, some background of quantum physics will be presented, followed by a few applications, and finally, the goals of the project in this thesis will be explained. Briefly, the goals are to design and fabricate two coupled superconducting resonators in the microwave regime, and to characterize such a system. Based on previous work in our field, we chose to perform parametric frequency conversion to suffice as a verification that the two coupled resonators perform as expected. We delimit the work in this thesis to that goal, and do not touch upon the subject of photonic condensates.

1.1 Quantum physics

The world of quantum physics contains several fundamental, non-intuitive phenomena. To think about these and utilize them in experiments one needs to try to develop at least some intuition by creating analogues and methods to visualize the theory. Some of the fundamental aspects of quantum mechanics are:

1. **Quantization.** Energy is quantized. This was discovered by Planck in 1900 [2], and elaborated on by Einstein in 1905 [3]. It means that energy comes in small packages and one example is the electron orbitals around the atomic nucleus in Bohr's model. The electronic energy is quantized in the sense that only certain radii of the orbitals are allowed. An analogue scaled to a macroscopic world could be that the possible speeds of which you could drive your car would only be to be 10, 20, 30 km/h, *etcetera*. You might have noticed the absence of 0 km/h. This was on purpose since in quantum mechanics nothing can be completely still or empty, there will always be vacuum fluctuations. But since energy is quantized in very small steps we do not notice it in our everyday life. This is why you usually need small features and low temperatures to observe quantum mechanical effects.

2. **Superposition.** In the quantum world, a system can be in two or more states at the same time. When you try to observe which state it is in, you will force the system to choose one of the states and this will be what you measure. This implies that your system is non-deterministic, i.e., even if you repeat an experiment using the exact same parameters, you can get a different result. Using the same analogue as before, it would be like the car was driving at both 20 and 30 km/h, at the same time. Then, when you measure what speed it is actually driving, you will force the car to choose one of the speeds and this will be what you measure. Superposition is one of the fundamental reasons why a quantum computer can achieve speed-up beyond what is classically possible.
3. **Entanglement.** Not only can a system be in two states at the same time, it can also be entangled with another system, and what you do to one of them, will affect the other one instantaneously, independently of the distance. The analogue would now be two cars, which are entangled in a certain way in a superposition between 20 and 30 km/h. Let us then measure the speed of car 1, and if the result is 20 km/h, then car 2 is automatically driving at 30 km/h, or *vice versa*. One might think that this would enable transfer of information faster than the speed of light, but this is not the case, since the person with the other particle must know exactly what you did to your particle, and hence a classical communication channel is required.
4. **Particle-wave dualism.** The fact that we can choose to look upon a object as either a particle or a wave, is both non-intuitive and very useful. Depending on the situation, e.g. when describing how light travels, it is advantageous to see it as a wave, but as soon as it collides with matter we change to the particle description with an associated position and momentum.

Eventually, we would like to perform our experiments in the quantum regime. However, most of the measurement results in this thesis can be explained by a classical model. But the road to the quantum regime is rather straightforward and will be pointed out when we discuss the outlooks of this project.

1.1.1 Quantum optics

Classical optics, the study of how light behaves in different media, e.g. air, glass and water, and how it interacts with matter, is usually what we think of when we hear the word optics. We can do similar studies, but in the quantum regime instead, meaning how single particles of light (photons) interact with matter (single atoms). This field of study is called quantum optics [4], and has been a hot topic in research for the last 100 years or so. Historically, one has studied the interaction between laser light in the optical regime, and ordinary atoms.

Isolating and locating single atoms is hard. However, since the discovery of superconducting qubits [5], which is an artificial nanoscale system with properties similar to real atoms, scientists are able to place a single "atom" at an arbitrary position. This enables very precise control over the atom and its couplings to other systems, e.g. light or other atoms [6, 7].

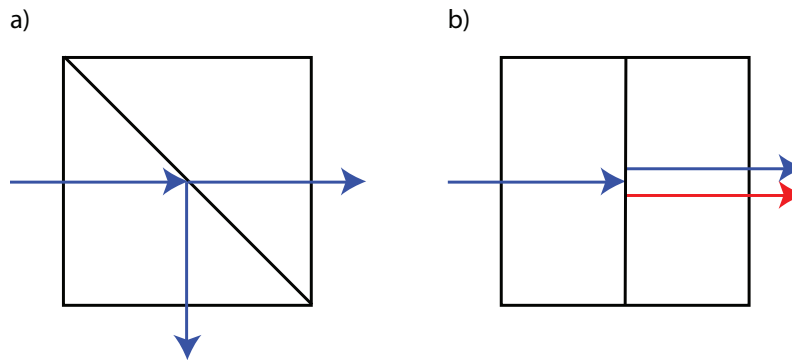


Figure 1.1: Illustration of the principle behind two optical devices. **a)** Beam splitter, one input that is split into two outputs. The color of the light is preserved **b)** Frequency converter, one input and one output, but the light is split into two different colors.

Many experiments in the settings of quantum optics utilize resonators for controlling light. A resonator can be thought of as a trap for light. When light is incident on the resonator, it gets absorbed, and stays there for some time before it leaks out again. One example with optical light is the Fabry–Pérot cavity, which consists of two parallel mirrors where light can bounce back and forth. The mirrors need to be of high quality, otherwise the light will just scatter, and after a few round trips, the light is lost. The distance between the two mirrors sets the frequency of which the light is bouncing back and forth (the number of round trips in one second), and is called the resonance frequency of the resonator.

In this work however, we use microwaves instead of optical light, and the resonators are therefore designed differently. They are fabricated on a small chip ($5 \times 7 \text{ mm}^2$), and there are no real mirrors in the sense of what we are used to – instead we use electrical circuits that are equivalent to the optical case. To make these circuits with very high qualities, we use superconductors, due to their low losses.

1.1.2 Quantum computing

A classical computer uses bits, i.e. two-level systems that are either 0 or 1, to encode information. However, if we have a quantum two-level system (qubit), we can use the phenomenon of superposition, to make the qubit be both in the 0 and the 1 state, at the same time [8]. This can be utilized to speed up calculations, if one can find an algorithm to transfer the problem onto the quantum system and taking advantage of its quantum properties. The two main research areas relating to quantum computing are: to find smart algorithms, and to build a controllable system with sufficiently many qubits of high quality [9].

It is possible to divide all qubits into two different categories: stationary qubits, and flying qubits. A flying qubit is a two-level system that is moving in space. Usually it is light (photons), but one could think of using also sound (phonons) [10]. The information is then encoded into e.g., the polarization of the light, or the frequency of it. The advantage of this method is that is easier to transfer the information around, since the qubits themselves are photons that move with the

speed of light, and it is possible to manufacture optical fibers with very low loss. However, photons do not like to interact with other photons, making it more difficult to actually perform calculations with them.

A stationary qubit is the opposite of a flying qubit. It is a two-level system that is fixed in a spatial location, and then controlled by some source of light usually, e.g. a laser or a microwave generator. Examples of stationary qubits are the transmon [11], quantum dots [12], and NV-centers in diamonds [13]. These can be easier to control, since you always know where the qubits are.

Another application of qubits is quantum simulation. On a classical computer it is only possible to simulate the simplest atoms and molecules, but with a clever design of a network with qubits, one can simulate more advanced systems, in a much shorter time [14].

1.2 Goals of this project

The goals of this project are to build two coupled superconducting resonators, and investigate parametric frequency conversion in such a device. This device works in the microwave regime, at frequencies between 4 and 8 GHz, but analogues can be made to the optical regime, for simpler understanding. If we, for example, would send blue light into such a device, we can get red light out, or a bit of both.

This can also be done in a quantum regime, where we would send in just one blue photon, which we can coherently swap between blue and red. We could even put it into a superposition of blue and red, which means that it will have both colors at the same moment. It is not until we observe its color, that it determines what color it has. This experiment was already done by Zakka-Bajjani, *et al.* in 2011 [15], but in a slightly different system. They used two modes in one resonator, whereas we will use the two modes of two coupled resonators in this project.

There are at least three different applications for a device like this. First, it can be used in the context of (quantum) optics. Because, as we will see later, the frequency conversion is described by the same equations as an optical beam splitter. A beam splitter is a device which, in the classical regime, can be used to split incoming light into two paths, see Figure 1.1 for a comparison between the beam splitter and the frequency converter. However, in the quantum regime with single photons – it will not split the photon, it will force it to go either one way or the other. In our device, it will not be two output paths, it will be two output frequencies.

Secondly, the device can be used directly for quantum computing, as flying qubits. If a photon (flying qubit) is incident on our device, we can do gates on this qubit by applying different pump schemes, e.g. flipping the state from 0 to 1, or putting it in a superposition of 0 and 1.

Thirdly, it can mediate information in a quantum computer using stationary qubits. One could, for example, use this device to first create entanglement between one stationary qubit and the resonator, and then to transfer the state of the resonator to a second stationary qubit, hence creating entanglement between the two qubits.

2

Theoretical descriptions

IN this chapter we introduce the theory that describes our devices and that explains the results of our measurements. Our focus is mainly on the physics of two coupled resonators, together with parametric frequency conversion, intended to create an understanding of the measurements performed in this work. These derivations will be explained more in detail, while the theory behind concepts such as superconductivity and microwave resonators will only be briefly outlined. Interested readers, or those new to the subject, can refer to basic textbooks, such as [16, 17]. We explain the bigger picture, and derive only the most important parts, and point out where to find more information and full derivations as we go along.

2.1 Superconductivity

As the word suggests, superconductivity is a phenomenon where the conductivity is very large. In fact it is infinite for DC (low frequencies), meaning exactly zero resistance. Superconductivity was first observed by H. K. Onnes in 1911, using mercury [18]. When the mercury was cooled down below a certain critical temperature T_c , he observed an abrupt decrease in resistance, by several orders of magnitude. As it turns out, this is not the only effect that happens in a superconductor, it also expels all magnetic field from its interior, called the Meissner effect [19]. For the first half of the 20th century, despite enormous efforts; there existed no microscopic theory for superconductivity, until in 1957 when Bardeen, Cooper and Schrieffer published the so called BCS-theory [20], eventually yielding them a Nobel-prize. In principle, their theory posits that two electrons inside the material can pair up due to an attractive interaction, and create a so-called Cooper-pair. Cooper-pairs, in contrast to electrons, are bosons; meaning that below a critical temperature, can condense into a single state and be described by a single wavefunction or order parameter $\Psi = \sqrt{n_s}e^{i\theta}$, where n_s is the density of Cooper pairs and θ the phase of the condensate. The Cooper-pairs can move without scattering inside the superconductor, hence giving rise to zero resistivity. More information about the BCS-theory and two phenomenological models, the London theory and the Ginzburg-Landau theory, can be found in [16]. The two phenomenological theories are very well suited for creating an understanding and intuition of how a superconductor can be used.

2.1.1 The Josephson effect

The Josephson effect is a phenomenon in a system of two superconductors, coupled by a tunneling barrier, where two coupled electrons (Cooper-pairs) tunnel through the barrier, without dissipating energy; hence it is possible to draw a current through this barrier without applying any voltage across it. This was first derived theoretically by Brian Josephson in 1962 [21], and observed experimentally by Anderson and Rowell the year after [22]. In the famous *Feynman Lectures on Physics* [23], Richard Feynman makes an elegant and more simplified derivation of the Josephson effect, which we outline in Appendix B. The result is two relations between current, voltage and phase across the junction

$$I = I_c \sin \varphi, \quad (2.1)$$

$$V = \frac{\hbar}{2e} \frac{d\varphi}{dt}, \quad (2.2)$$

where I_c is the critical current of the junction, V is the voltage and φ the phase difference across the same. If we differentiate (2.1) and use it together with (2.2) we arrive at

$$V = \frac{\hbar}{2e} \frac{1}{I_c \cos \varphi} \frac{dI}{dt}. \quad (2.3)$$

Recalling the voltage-current relation for an inductance, $V = L dI/dt$, we can define the Josephson inductance from (2.3) as

$$L_J = \frac{\hbar}{2e} \frac{1}{I_c \cos \varphi} \quad (2.4)$$

However, the Josephson relations can be further extended to include more general Bose-Einstein condensates [24]. It has been observed, for example, in superfluid helium-4 [25], laser-cooled atoms [26], and excitation-polariton systems [27]. If one were able to create two coupled photonic condensates, there should also be a photonic Josephson current, obeying the Josephson relations.

2.1.2 SQUID

A superconducting quantum interference device (SQUID) consists of two Josephson junctions in a loop, as illustrated in figure 2.1. Assuming identical junctions, i.e. the same critical current, we can modify (2.1) to

$$I = 2I_c \cos \left(\pi \frac{\Phi}{\Phi_0} \right) \sin \varphi, \quad (2.5)$$

where Φ is the magnetic flux through the SQUID loop and $\Phi_0 = h/(2e)$ is the magnetic flux quantum. For a symmetric SQUID one usually drops the factor 2 and redefines I_c to mean the critical current of the SQUID (two impedances in parallel). The most important feature of the SQUID is that the effective critical current can be tuned by changing the magnetic flux through the loop. This also implies that the formula for the Josephson inductance gets modified to

$$L_J = \frac{\hbar}{2e} \frac{1}{I_c |\cos(\pi\Phi/\Phi_0)| \cos \varphi}. \quad (2.6)$$

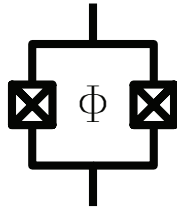


Figure 2.1: Illustration of a SQUID. It consists of two Josephson junctions (represented as squares with a cross) in parallel, effectively forming a loop. Φ denotes the magnetic flux through this loop.

The SQUID was first demonstrated in 1964 by Jaklevic *et al.* [28], and for a comprehensive review, see [29].

The fact that the SQUID's current and voltage is sensitive to a small fraction of a single flux quantum is used in several different applications today. First of all, it is a very sensitive magnetometer with applications in medicine, e.g. as detectors in MRI and MEG. Since the inductance of the SQUID is highly non-linear due to the cosine dependence of φ , it is used to modify a harmonic oscillator into an anharmonic one, introducing the ability to isolate only two energy levels of the oscillator, hence creating a quantum bit or qubit. Qubits are the fundamental building blocks for quantum computers, and superconducting qubits are one of the most promising architectures for building such a system [5, 30].

Due to the geometry of the SQUID, there is also some capacitance in parallel with the inductance from equation (2.6). This creates an LC resonator, with resonance frequency around 40 GHz. We need to operate below this frequency if we want the SQUID to behave as an inductor.

2.2 Transmission lines and resonators

A transmission line is used to guide electromagnetic waves (light) from one point to another. There are many different types of transmission lines, the most common ones being the coaxial cable, microstrips, and co-planar waveguides. A transmission line can be described by the telegraph equations [17], which uses that the transmission line carries some inductance per unit length, L_0 , and some capacitance per unit length, C_0 . The impedance seen by an incoming wave sees, is called the characteristic impedance of the transmission line, and is denoted by Z_c . For a lossless transmission line we have $Z_c = \sqrt{L_0/C_0}$.

2.2.1 Resonators

Many experiments in quantum computing and quantum optics using superconducting qubits also utilize a superconducting resonator to store photons [31, 32], achieve strong coupling to qubits [6, 33] and parametrically amplify signals with quantum-limited noise [34].

When working with something that oscillates, it is always good, from a pedagogical point of view, to make the analog with an ordinary mechanical pendulum,

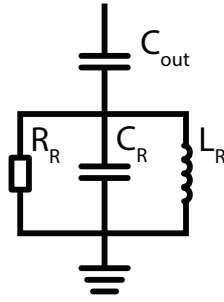


Figure 2.2: An electrical resonator coupled to a transmission line. The resonance frequency is given by $\omega_r = 1/\sqrt{L_R C_R}$. R_R describes the losses inside the resonator.

e.g. a swing. A simple pendulum, i.e. a massive object attached to a massless rod, is described for small oscillations by the differential equation of a harmonic oscillator

$$\frac{d^2x}{dt^2} + 2\Gamma \frac{dx}{dt} + \omega_r^2 x = F(t), \quad (2.7)$$

where x is the angle of the pendulum relative to its resting position, Γ is the damping of the system, ω_r the resonance frequency and $F(t)$ is an external driving force. In the case of a pendulum we can express the resonance frequency as $\omega_r^2 = \frac{g}{l}$ where g is the acceleration due to gravity and l is the length of the rod.

However, in our case ω_r is the resonance frequency of an electrical circuit, the damping Γ is the total loss rate of signal, both external and internal, and the driving force $F(t)$ is the applied signal. External loss, Γ_0 , refers to the signal that leaks back to the transmission line used to probe the resonator, whereas internal loss, Γ_i , is signal lost inside the resonator due to some imperfections. When $\Gamma_0 > \Gamma_i$, the system is overcoupled, meaning that more signal is leaking out to the transmission line, than what is lost inside. $\Gamma_0 = \Gamma_i$ is called critically coupled, and $\Gamma_0 < \Gamma_i$ is called undercoupled. Usually we prefer to work in the overcoupled regime, since the signal that leaks out into the transmission line is measurable.

An electrical resonator can be described as an inductance L_R in parallel with a capacitance C_R , see Figure 2.2. The resonance frequency is then given by $\omega_r = 1/\sqrt{L_R C_R}$. To model the internal loss, we add a resistor R_R to the circuit. To probe the resonator we add a capacitance C_{out} in series with the resonator, this gives the external loss rate. Instead of talking of loss rates, one can instead use quality factors. The quality factor is the amount of oscillations needed for the signal to decrease to $1/e$ of its inertial value. We define the internal and external quality factors as $Q_i = f_r/2\Gamma_i$ and $Q_e = f_r/2\Gamma_0$, respectively, and relate these to the circuit parameters in the following way

$$Q_i = f_r R_R (C_R + C_{\text{out}}), \quad (2.8)$$

$$Q_e = \frac{C_R + C_{\text{out}}}{Z_0 C_{\text{out}}^2 f_r}. \quad (2.9)$$

If we send in a signal to the resonator described above, we can measure the reflection of this signal, S_{11} . The reflected signal is equal to

$$S_{11} = \frac{Z_r - Z_0}{Z_r + Z_0} = \frac{\Delta - i(\Gamma_i - \Gamma_0)}{\Delta - i(\Gamma_i + \Gamma_0)} = \frac{\Delta^2 + \Gamma_i^2 - \Gamma_0^2 + i2\Delta\Gamma_0}{\Delta^2 + (\Gamma_i + \Gamma_0)^2}, \quad (2.10)$$

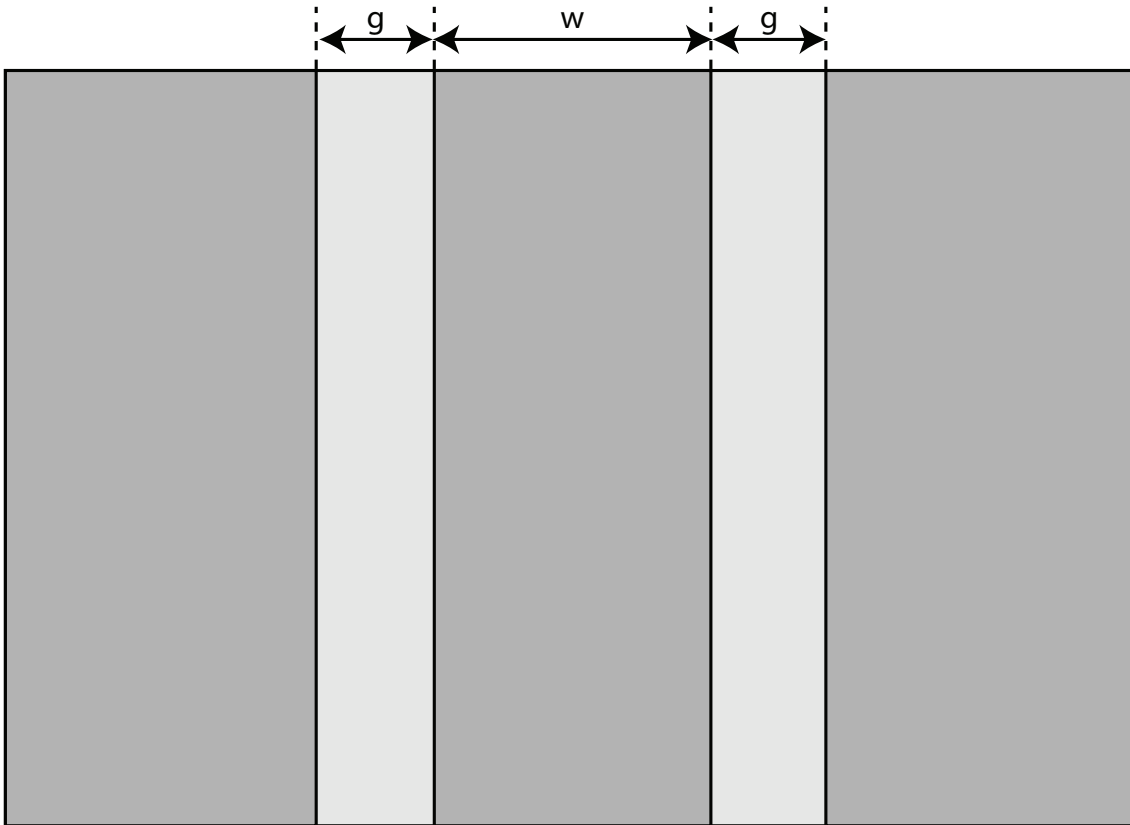


Figure 2.3: A schematic of the co-planar waveguide. w is the width of the center conductor and g is the gap between the center conductor and the ground planes.

where Z_r is the impedance of the resonator, Z_0 the characteristic impedance of the transmission line (50Ω), and Δ the detuning from the resonance frequency f_r .

2.2.2 Co-planar waveguides

So far we only talked about transmission lines and resonators in terms of theory, assuming there is a system described with the equations in previous sections. Here, we introduce the transmission line used in this work, namely the co-planar waveguide (CPW) [35], which has been used extensively in both normal and superconducting circuits. The most simple description of the CPW is to have a coaxial cable, and take a cross-section through the center, i.e. it is a center strip of metal of width w , surrounded by two ground planes with some gap distance, g , to the center conductor, as shown in Figure 2.3. These two widths determine the inductance and capacitance per unit length.

As we saw before, a transmission line has a characteristic impedance Z_c . The most common Z_c for microwave equipment is 50Ω , thus we need to design our CPW to also have this to avoid unwanted reflections at the interfaces. The characteristic impedance is given by $Z_c = \sqrt{L_0/C_0}$, where L_0 and C_0 are the inductance and capacitance per unit length of the CPW, respectively. The phase velocity of the light in the CPW is given by $v_{\text{ph}} = 1/\sqrt{L_0C_0}$.

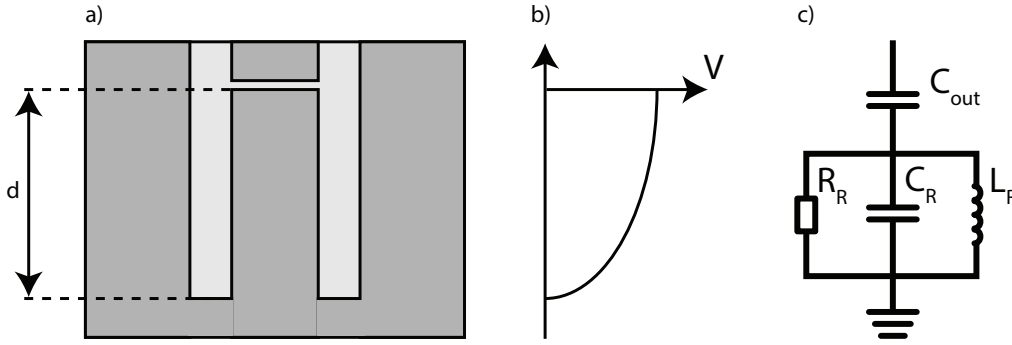


Figure 2.4: $\lambda/4$ resonator based on a CPW. **a)** Illustration of the resonator. At the top is the coupling capacitor, and at the bottom the center conductor is shorted to the ground planes. Not to scale, d is usually orders of magnitude larger than both the width of the center conductor and the width of the gaps. **b)** Electric potential as a function of the position inside a $\lambda/4$ resonator. **c)** Equivalent circuit close to resonance.

To create a resonator out of a CPW, we ground it at one end, and put a capacitor at the other, shown in Figure 2.4 a. The distance, d , between these two points is then equal to a quarter of the wavelength, corresponding to the resonance frequency, Figure e 2.4 b. Hence, we call it a $\lambda/4$ resonator. Close to resonance, we can treat the resonator as a lumped-element LC-resonator, Figure 2.4 c, with the resonance frequency

$$f_{\lambda/4} = \frac{v_{\text{ph}}}{4d} = \frac{1}{4d\sqrt{L_0C_0}} = \frac{1}{2\pi\sqrt{L_R C_R}}, \quad (2.11)$$

where $L_R = 8dL_0/\pi^2$ and $C_R = 2dC_0/2$ are the lumped element equivalent inductance and capacitance of the resonator, respectively. R_R corresponds to the losses inside the resonator.

Since the resonance frequency is also dependent of L_0 and C_0 , which are determined by the design of the CPW, the design will determine both the characteristic impedance and the resonance frequency of the resonator.

2.2.3 Tunable resonators

The resonators described above are fixed in frequency, in some applications this is sufficient. However, in this project, a tunable resonance frequency is necessary for two reasons: first, we should be able to tune it statically to a desired working frequency. Secondly, it allows for fast modulation around this working frequency. This modulation can even be faster than the resonance frequency, if desired.

To introduce these properties we add a SQUID at the grounding point. From an electrical circuits point of view this will add an inductance in series with the LC-resonator, when close to resonance. Since the resonance frequency is dependent on the total inductance, it is now also dependent on the magnetic flux through the SQUID. The resonance frequency of the resonator terminated by the SQUID is well

approximated by [36, 37]

$$f_r(F) \approx \frac{1}{2\pi\sqrt{(L_r + L_s(F))C_r}} \approx \frac{f_{\lambda/4}}{1 + \gamma_0/|\cos(F)|}, \quad (2.12)$$

where $F = \pi\Phi_{dc}/\Phi_0$, and $f_{\lambda/4}$ is the bare resonance frequency, meaning the resonance frequency that the resonator would have without the SQUID. γ_0 is the inductive participation ratio, defined as $\gamma_0 = L_J/L_r$, the Josephson inductance of the SQUID, divided by the inductance of the resonator.

Adding a SQUID to the resonator not only enables frequency modulation, both statically and dynamically, but it also adds a non-linearity to the system due to the cosine dependence of the phase φ across the junction in equation (2.6). By Taylor expanding this term to second order, we get a cubic term in the equation of motion for the oscillator, equation (2.7). This non-linearity is called the Duffing non-linearity, since it gives the resonance the shape of a Duffing oscillator [38]. The Duffing term introduces a frequency shift of the resonance frequency, depending on the current through the SQUID, which is proportional to the number of photons in the resonator. The frequency shift is quantified with the parameter α , which is the frequency shift per photon in the resonator. As hinted above, it also changes the lineshape of the resonance, depicted and analyzed more in [39].

2.2.4 Two coupled resonators

If we couple two resonators, (A) and (B), with the same resonance frequency together, two new resonances emerge symmetrically around the original resonance frequency, this is called hybridization. The two new resonance frequencies, f_1 and f_2 , are given by [32]

$$f_{1,2} = \frac{f_A + f_B}{2} \pm \sqrt{J^2 + \left(\frac{f_A - f_B}{2}\right)^2}, \quad (2.13)$$

where f_A and f_B are the resonance frequencies of each resonator, and J is the coupling strength between them. In this work we denote the higher mode 1. When the detuning $|f_A - f_B|$ is much larger than the coupling J , equation (2.13) gives the two original frequencies, f_A and f_B , hence there is no interaction between the two resonators. For zero detuning, the two resonance frequencies are split by $2J$.

For two tunable resonators, we use equation (2.12), together with (2.13), to get an expression for the resonance frequencies as a function of magnetic flux in each SQUID.

To go from an equivalent electrical circuit, Figure 2.5, for the two coupled resonators to something we can measure, i.e. S-parameters, we use the ABCD-matrices. The advantage of using them is that if we want to cascade several two-port networks, we just use matrix multiplication. The ABCD-matrix relates the currents and the voltages of a two-port network in the following way

$$\begin{pmatrix} V_1 \\ I_1 \end{pmatrix} = \begin{pmatrix} A & B \\ C & D \end{pmatrix} \begin{pmatrix} V_2 \\ I_2 \end{pmatrix}. \quad (2.14)$$

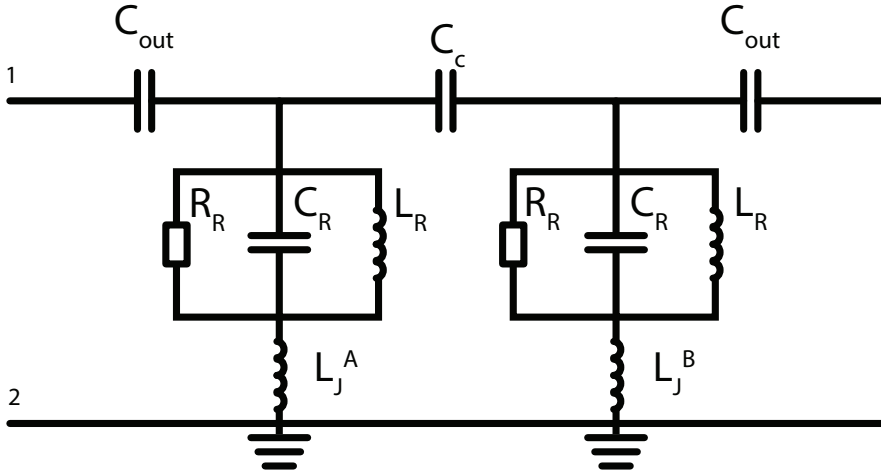


Figure 2.5: Equivalent electrical circuit for two coupled $\lambda/4$ resonators each terminated by a SQUID, close to resonance. 1 and 2 denotes the reference ports used in the ABCD-matrix calculation.

We draw the equivalent circuit for the two coupled resonators as in Figure 2.5. Each series impedance Z we write as

$$\begin{pmatrix} A & B \\ C & D \end{pmatrix} = \begin{pmatrix} 1 & Z \\ 0 & 1 \end{pmatrix}, \quad (2.15)$$

and for each shunt admittance Y

$$\begin{pmatrix} A & B \\ C & D \end{pmatrix} = \begin{pmatrix} 1 & 0 \\ Y & 1 \end{pmatrix}. \quad (2.16)$$

For the two coupled resonators this yields the following ABCD-matrix

$$\begin{pmatrix} A & B \\ C & D \end{pmatrix} = \begin{pmatrix} 1 & 1/i\omega C_{\text{out}} \\ 0 & 1 \end{pmatrix} \begin{pmatrix} 1 & 0 \\ Y_A & 1 \end{pmatrix} \begin{pmatrix} 1 & 1/i\omega C_c \\ 0 & 1 \end{pmatrix} \begin{pmatrix} 1 & 0 \\ Y_B & 1 \end{pmatrix} \begin{pmatrix} 1 & 1/i\omega C_{\text{out}} \\ 0 & 1 \end{pmatrix}, \quad (2.17)$$

with $Y_{A/B} = 1/i\omega(L_R + L_J^{A/B}) + i\omega C_R + 1/R_R$, assuming identical resonators, and where $L_J^{A/B}$ are the Josephson inductances of each SQUID depending on the flux through the loop, as given in equation (2.6). The coupling strength between the two resonators are set by the capacitance C_c .

The ABCD-matrix can then be converted to S-parameters using simple relations [17], e.g. the reflection at resonator (A) is

$$S_{AA} = \frac{A + B/Z_0 - CZ_0 - D}{A + B/Z_0 + CZ_0 + D}, \quad (2.18)$$

where Z_0 is the impedance of the transmission lines used to probe the resonators.

It might be interesting to know how the electric field of the two modes are distributed inside the resonators, when the detuning is zero. Following the method developed in [40], and expanded to two resonators in [41], we arrive at the plot in Figure 2.6. We see an odd and an even mode, with slightly different frequencies. The derivation leading up to these results are performed in Appendix C.

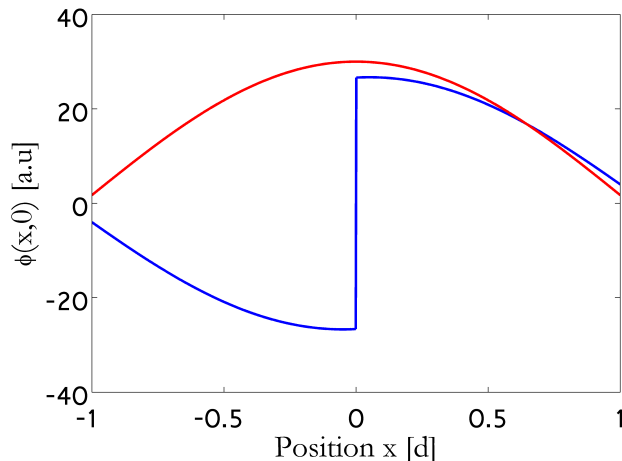


Figure 2.6: Mode structures for two identical, coupled, $\lambda/4$ cavities, each terminated by a SQUID, c.f. Figure 2.5. Plotted is the superconducting phase, as a function of position inside the resonators, in units of d , the length of one resonator. The coupling capacitor C_c is located at $x = 0$.

2.3 Parametric pumping

Parametric pumping refers to the pumping (modulation) of one of the parameters of a system. In the case with a resonator we have two possibilities, to modulate the damping or the resonance frequency. When placing a SQUID at the end of the resonator we get a resonator with a tunable resonance frequency. By modulating the magnetic field with a sinusoidal signal, we get a modified version of equation (2.7):

$$\frac{d^2x}{dt^2} + 2\Gamma \frac{dx}{dt} + (\omega_r^2 + \epsilon^2 \cos(\omega_p t)) x - \alpha x^3 = F(t), \quad (2.19)$$

where ω_p is the angular frequency that modulate the resonance frequency, ϵ is the amplitude of the variation, and α is the Duffing term. This problem can, in some situations, be treated via quantum network theory [42, 43] or the method of slow variables [44]. Slow variables refers to that the amplitude of the oscillations in the resonator is changing much slower than the oscillations themselves.

Another solution to this problem was developed by Wustmann and Shumeiko [40]. They use a resonator field amplitude formalism, where they describe the amplitude of the field inside the resonator with a parameter A . Then, they derive a simplified Langevin equation of the resonator, when using various parametric pumping conditions. For example, they treat the cases of parametric amplification and parametric oscillations. For a comparison between the different methods for treating parametric pumping, see [45].

2.3.1 Frequency conversion

The theory for parametric effects with just one resonance can be further developed to a multimode case, where the signal and the idler lie in two different modes, in

contrast to the single-mode case where they are at the same frequency. This can be utilized for multimode parametric amplification [46], where power is converted from one frequency to another via the nonlinear interaction. In a quantum picture, a pump photon splits into two, one in each mode, $f_p = f_1 + f_2$, i.e. three-wave mixing or parametric down-conversion.

One could also pump at the difference frequency between two modes $f_p = f_1 - f_2$, rather than the sum as described above. This will lead to parametric up-conversion, where the pump photon and a photon at mode 1 will combine and create a photon at mode 2, or *vice versa*. As we will see, the outcome of this is very similar to that of an optical beam splitter, but instead of splitting an incoming beam into two spatially separated beams, the parametric conversion splits the incoming wave into two frequency-separated waves.

Here, we derive the input-output equations for the parametric frequency conversion, using the resonator field amplitude formalism. We define the pump frequency as $f_p = f_1 - f_2 + 2\delta$ where $f_1 > f_2$ are the cavity eigenmodes. The relations between the original fields, a_j , inside the resonator, and the slow amplitudes, A_j , are

$$a_1(t) = A_1(t)e^{-i2\pi(f_1+\delta)t}, \quad (2.20)$$

$$a_2(t) = A_2(t)e^{-i2\pi(f_2-\delta)t}. \quad (2.21)$$

Thus the dynamical equations for the field inside the cavities A_j are

$$i\dot{A}_1 + \zeta A_1 + i(\Gamma_i^{(1)} + \Gamma_0^{(1)})A_1 + \epsilon A_2 = \sqrt{2\Gamma_0^{(1)}}B_1(t), \quad (2.22)$$

$$i\dot{A}_2 + \zeta A_2 + i(\Gamma_i^{(2)} + \Gamma_0^{(2)})A_2 + \epsilon A_1 = \sqrt{2\Gamma_0^{(2)}}B_2(t). \quad (2.23)$$

We see that A_2 is coupled to A_1 via the parametric pump strength ϵ , and *vice versa*. ζ_j are the pump-mode detunings including the Duffing non-linearity,

$$\zeta_1 = \delta + \alpha_1|A_1|^2 + 2\sqrt{\alpha_1\alpha_2}|A_2|^2, \quad (2.24)$$

$$\zeta_2 = \delta + \alpha_2|A_2|^2 + 2\sqrt{\alpha_1\alpha_2}|A_1|^2. \quad (2.25)$$

B_j are the slow amplitudes of the input-fields given by

$$b_1(t) = B_1(t)e^{-i2\pi(f_1+\delta)t}, \quad (2.26)$$

$$b_2(t) = B_2(t)e^{-i2\pi(f_2-\delta)t}, \quad (2.27)$$

where b_j are the original input fields. The slow amplitudes of the output fields C_j are expressed as,

$$C_j(t) = B_j(t) - i\sqrt{2\Gamma_j^0}A_j(t). \quad (2.28)$$

Now, consider that the input signal is detuned by Δ from $f_1 + \delta$ and $f_2 - \delta$, and that the system has reached its steady state, meaning $\dot{A}_j = 0$. This modifies (2.22) and (2.23) to

$$(\Delta + \zeta_1 + i(\Gamma_i^{(1)} + \Gamma_0^{(1)}))A_1 + \epsilon A_2 = \sqrt{2\Gamma_0^{(1)}}B_1, \quad (2.29)$$

$$(\Delta + \zeta_2 + i(\Gamma_i^{(2)} + \Gamma_0^{(2)}))A_2 + \epsilon A_1 = \sqrt{2\Gamma_0^{(2)}}B_2. \quad (2.30)$$

These two coupled equations have the solution

$$\begin{pmatrix} A_1 \\ A_2 \end{pmatrix} = \frac{1}{\text{Det}} \begin{pmatrix} \Delta + i(\Gamma_i^{(2)} + \Gamma_0^{(2)}) + \zeta_2 & -\epsilon \\ -\epsilon & \Delta + i(\Gamma_i^{(1)} + \Gamma_0^{(1)}) + \zeta_1 \end{pmatrix} \begin{pmatrix} \sqrt{2\Gamma_0^{(1)}} B_1 \\ \sqrt{2\Gamma_0^{(2)}} B_2 \end{pmatrix}, \quad (2.31)$$

with the determinant $\text{Det} = (\Delta + i(\Gamma_i^{(1)} + \Gamma_0^{(1)}) + \zeta_1)(\Delta + i(\Gamma_i^{(2)} + \Gamma_0^{(2)}) + \zeta_2) - \epsilon^2$. Doing input-output theory we arrive at

$$\begin{pmatrix} C_1 \\ C_2 \end{pmatrix} = \hat{V} \begin{pmatrix} B_1 \\ B_2 \end{pmatrix}, \quad (2.32)$$

with the input-output matrix elements

$$V_{11} = 1 - \frac{2i\Gamma_0^{(1)}(\Delta + i(\Gamma_i^{(2)} + \Gamma_0^{(2)}) + \zeta_2)}{\text{Det}}, \quad (2.33)$$

$$V_{22} = 1 - \frac{2i\Gamma_0^{(2)}(\Delta + i(\Gamma_i^{(1)} + \Gamma_0^{(1)}) + \zeta_1)}{\text{Det}}, \quad (2.34)$$

$$V_{12} = \frac{i2\epsilon\sqrt{\Gamma_0^{(1)}\Gamma_0^{(2)}}}{\text{Det}}, \quad (2.35)$$

$$V_{21} = V_{12}. \quad (2.36)$$

These are exact non-linear formulas containing the Duffing shift but not the pump-induced frequency shift of δ [40, 39].

Assuming weak signals and neglecting the Duffing correction, $\zeta_1 \rightarrow \delta$ and $\zeta_2 \rightarrow -\delta$, we can express equations (2.33)-(2.36) as

$$V_{11} = \frac{(\Delta + \delta + i(\Gamma_i^{(1)} - \Gamma_0^{(1)}))(\Delta - \delta + i(\Gamma_i^{(2)} + \Gamma_0^{(2)})) - \epsilon^2}{(\Delta + \delta + i(\Gamma_i^{(1)} + \Gamma_0^{(1)}))(\Delta - \delta + i(\Gamma_i^{(2)} + \Gamma_0^{(2)})) - \epsilon^2}, \quad (2.37)$$

$$V_{22} = \frac{(\Delta + \delta + i(\Gamma_i^{(1)} + \Gamma_0^{(1)}))(\Delta - \delta + i(\Gamma_i^{(2)} - \Gamma_0^{(2)})) - \epsilon^2}{(\Delta + \delta + i(\Gamma_i^{(1)} + \Gamma_0^{(1)}))(\Delta - \delta + i(\Gamma_i^{(2)} + \Gamma_0^{(2)})) - \epsilon^2}, \quad (2.38)$$

$$V_{12} = \frac{i2\epsilon\sqrt{\Gamma_0^{(1)}\Gamma_0^{(2)}}}{(\Delta + \delta + i(\Gamma_i^{(1)} + \Gamma_0^{(1)}))(\Delta - \delta + i(\Gamma_i^{(2)} + \Gamma_0^{(2)})) - \epsilon^2}, \quad (2.39)$$

$$V_{21} = V_{12}. \quad (2.40)$$

These formulas contain two resonances, at $\Delta = \pm\delta$, i.e. the two original eigenmodes hybridize into four because of the pumping. At $\delta = 0$ they would formally cross, but finite ϵ produces an avoided crossing. At $\delta = 0$ and in the absence of internal loss, the distance between the hybridized modes is equal to 2ϵ . At this point the frequency conversion is perfect, meaning $|V_{11}| = |V_{22}| = 0$ and $|V_{12}| = |V_{21}| = 1$, however, a finite internal loss will reduce the efficiency. The two cases are shown in figure 2.7 **a**. We define the efficiency of the parametric frequency conversion as the maximum value of the magnitude of V_{21} . For lossless resonators, it is always unity, but decreases for finite internal loss. In Figure 2.7 **b**, we plot the efficiency as a function of the ratio between internal and external loss rates.

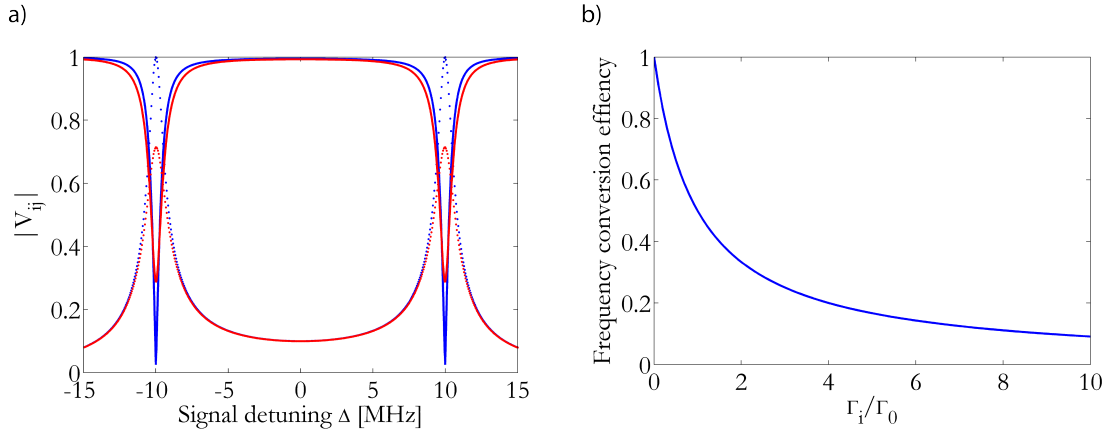


Figure 2.7: Matrix elements for frequency conversion. **(a)** Zero and finite internal loss. Blue lines are for $\Gamma_i^{(1)} = \Gamma_i^{(2)} = 0$, while red represents a finite internal loss $\Gamma_i^{(1)} = \Gamma_i^{(2)} = 0.2\Gamma_0^{(1)}$. Solid lines are $|V_{11}|$ and dotted lines $|V_{12}|$. For all traces $\epsilon = 10\Gamma_0^{(1)} = 10\Gamma_0^{(2)}$. **(b)** Frequency conversion efficiency, $\max(|V_{12}|)$, as a function of the ratio between internal and external loss, assuming identical resonators.

One can verify that $|V_{11}|^2 + |V_{12}|^2 = 1$, $|V_{11}| = |V_{22}|$ and $|V_{12}| = |V_{21}|$ for zero internal loss. This guarantees that the number of photons is conserved during the frequency conversion. As seen in figure 2.7 **a**, as expected, this is not the case for finite internal loss, since the definition of the internal loss itself is that photons are lost.

As briefly introduced in the previous chapter and illustrated in Figure 1.1, parametric frequency conversion and optical beam splitting is similar. A lossless optical beam splitter is described by

$$\begin{pmatrix} E_c \\ E_d \end{pmatrix} = \begin{pmatrix} r_{ac} & t_{bc} \\ t_{ad} & r_{bd} \end{pmatrix} \begin{pmatrix} E_a \\ E_b \end{pmatrix}, \quad (2.41)$$

where E_a and E_b are the input electric fields, and E_c and E_d are the output electric fields. r and t , are the reflectance and transmittance through a certain path in the beam splitter. The r and t matrix obey $|r_{ac}|^2 + |t_{ad}|^2 = 1$, $|r_{ac}| = |r_{bd}|$, and $|t_{bc}| = |t_{ad}|$, the exact same relations as for the input-output matrix of the parametric frequency conversion. Hence, we can talk about frequency conversion as a beam-splitting -like operation.

3

Experimental methods

WORKING in an experimental environment is a constant battle of problem solving. It follows a certain path, with some smaller or larger detours as you keep working against the goal. The goal is usually to observe some effect that has been described theoretically. At least this is the idea from the beginning, but as the project goes on, one might find that the results do not agree with the theoretical prediction, so then one needs to go back and modify the theory or the design of the device. This means that the process is an iterative one, which in general contains four steps:

1. **Modeling and designing the samples.** A very important step to put the device parameters in the correct regime, where the theory predicts interesting results.
2. **Device fabrication.** Here we try to realize the design from step 1. Depending on the level of difficulty of the clean room processes involved, this step can take from a few days, to several years.
3. **Measurement.** When we have our device, we need to test if it behaves as expected. This step begins with designing a measurement setup that allows us to measure what we are interested in. This might include cryogenics, wiring of RF- and DC cables, installation of magnets, *etcetera*.
4. **Data analysis.** What did the measurement tell us? Is it what we expect and how can we modify the design to improve the device's performance? Or do we need to modify the theory? Sometimes there is something completely new in the results, which no one had thought of before, and a completely new theory needs to be developed.

These four steps are repeated until the measurements and its analysis is satisfactory. Even though the process can be described quite generally, each project has its own problems and solutions. In one project the fabrication step might last for two years, while in another one the fabrication is easy, but the measurements are not. It might be hard to predict which step is going to take the most time beforehand, since each project is unique. Here we go through the basics of the three first steps, and how they are implemented in our device.

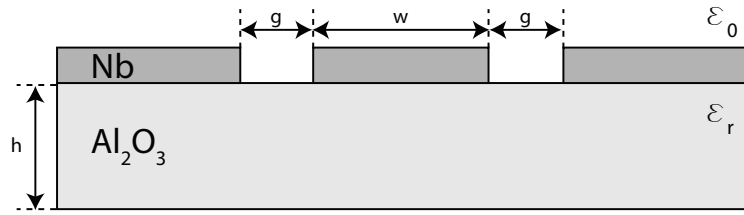


Figure 3.1: Illustration of a co-planar waveguide (CPW). In this work the substrate is made of sapphire (Al_2O_3), with a relative dielectric constant $\epsilon_r = 9.3$. The metal is niobium, and the center conductor width $w = 15 \mu\text{m}$, and a gap width $g = 6 \mu\text{m}$. Above the CPW is only vacuum, with the relative dielectric constant 1.

Table 3.1: Input (to the left) and output (to the right) parameters of the conformal mapping method [1], used to simulate a co-planar waveguide.

w	g	ϵ_r	h	ϵ_{eff}	v_{ph}	C	L	Z_0
$15 \mu\text{m}$	$6 \mu\text{m}$	9.3	$330 \mu\text{m}$	5.15	0.44 c	148.7 pF/m	385.1 nH/m	50.9Ω

3.1 Simulations and device modeling

Even though simulations does not always give very precise results, modeling and computer simulations are important to gives us an idea of how to design the samples, and what results to expect. We can split the modeling into two part: the first step is to model the physics with a theory, i.e., what parameters do we need. The second step is, how do we achieve these parameters?

Using the theory presented in the previous chapter, we can simulate what circuit parameters are needed for the two coupled superconducting resonators, in order to observe interesting results, e.g. frequency conversion.

To achieve these parameters, we start by designing the co-planar waveguides (CPW) that constitute our transmission lines and the two resonators. The definition of the relevant parameters are shown in Figure 3.1, and as seen in section 2.2.2, the width of the center conductor, and the widths of the gaps in the CPW, will determine characteristic impedance, $Z_0 = \sqrt{L/C}$, of the CPW. This impedance we would like to be as close to 50Ω as possible, to avoid reflections at the interfaces to the 50Ω coaxial cables. To simulate the required widths, we use the method of conformal mapping [1], a transformation, used in complex calculus, that preserves angles locally. Here it is used to transform the geometry of a CPW to that of a parallel plate capacitor, whose capacitance is well known and easy to calculate. The advantage of this method, is that is provides us with analytical expressions for the capacitance and inductance per unit length of the CPW. The input parameters to the conformal mapping, are the width of the center conductor, w , the width of the gap, g , the effective dielectric constant of the substrate, ϵ_r , and its thickness, h . The parameters used in this project, and the result of the conformal mapping, are found in Table 3.1.

Next, we simulate the capacitance of the input ports, and also the capacitance between the two resonators. This is done in the software Microwave Office, which

uses finite-element methods to solve Maxwell's equations, in a geometry defined by the user. In this project we use inter-digital finger structures, seen in Figure 3.2 c. This design provides large "contact" areas between the two electrodes, but in a small area of the sample. To simulate these structures in Microwave Office, we simply draw the geometry, and define the properties of the materials used; since there is no superconductor in the program, we instead use a perfect electrical conductor. However, these simulations unfortunately do not give accurate absolute numbers for the capacitance, but the relative number between two designs does agree to some extent. This means that if we simulate, fabricate, and measure one capacitor, we can use that as a reference for all future designs, as long as the capacitances of the new capacitors are roughly of the same order of magnitude as the the capacitance of the reference capacitor.

3.2 Fabrication

We fabricated the two coupled resonators in a state-of-the-art clean room, *the Nanofabrication Laboratory* at Chalmers University of Technology. Here we introduce the techniques and main ideas that are used on a daily basis for fabrication of nano devices. More details of the processes are found in [45], and the recipes used in this work are found in appendix A.

Our devices are fabricated on a 2", c-plane sapphire substrate, due to its low dielectric losses, hence, yielding high internal quality factors of the resonators. First, a thin film of niobium (80 nm) is sputtered onto the substrate, covering its entire surface. Then photolithography is used to define contact pads and alignment marks. These consists mainly of gold (80 nm), but with a layer of titanium (3 nm) beneath, to increase the adhesion between niobium and gold. Both the titanium and the gold are evaporated in the same vacuum cycle, using an electron-beam evaporator.

Next, electron-beam lithography is performed to define the co-planar waveguides in the niobium. Since this is an etching process, we expose the areas that should not have niobium, using a positive resist. Example of such an area, is the gap between the center conductor and the ground plane in the CPW. The lithography is followed by an inductively coupled plasma etch using NF_3 gas, which etches niobium but not sapphire, making the etching process fairly simple, since there is no critical timing issues.

The last part of the fabrication is to create the SQUIDs and divide the wafer into 24 individual samples. This is done by first using electron-beam lithography together with a bilayer resist system, to pattern two rectangles, separated by a short distance (250 nm), creating a so called Dolan-bridge [47]. We then dice the wafer into $5 \times 7 \text{ mm}^2$ samples using a saw with a diamond blade.

Then, the resists on the chips are developed one-by-one. One chip at the time is then inserted into a electron-beam evaporator only equipped with aluminum targets, ensuring that the targets and the chamber are kept as clean as possible. Inside the vacuum chamber there is also an ion gun used to etch away the native niobium-oxide before evaporation, to improve the contact between the niobium and the aluminum. To create the three parts of the Josephson junctions, we use a sequence of two evaporations, with an oxidation step in between. The first evaporation is done from

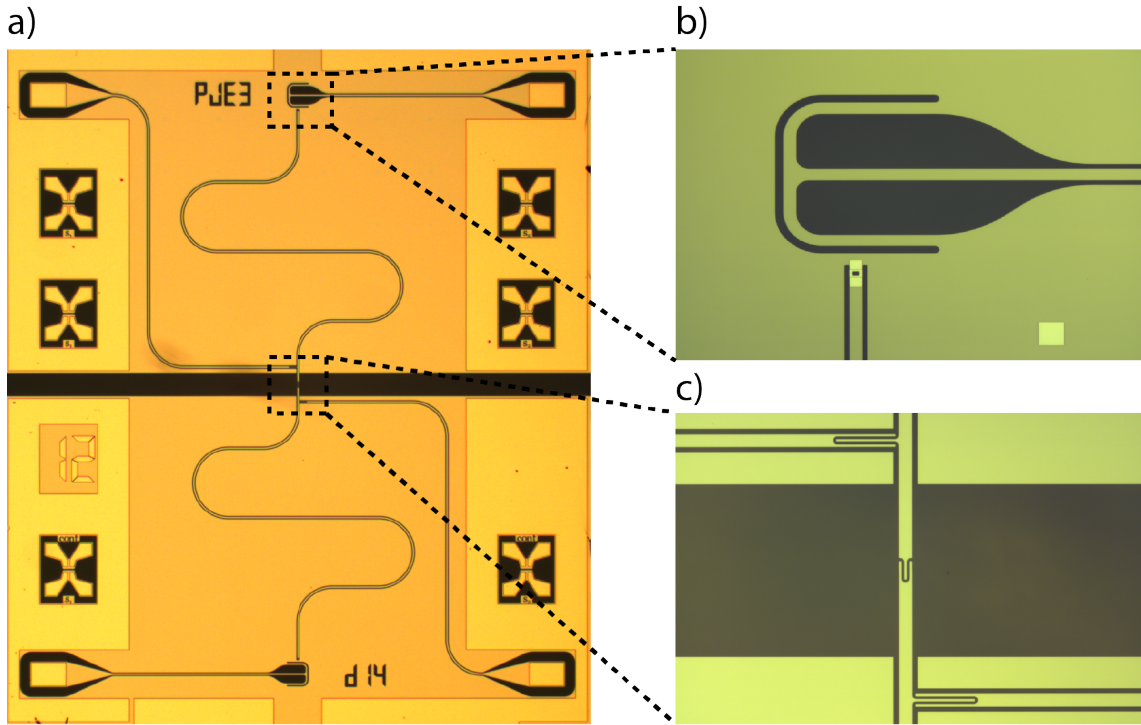


Figure 3.2: Micrographs of the fabricated sample used in this project. **(a)** Two capacitively coupled $\lambda/4$ resonators, each terminated by a SQUID, with their flux lines for DC-tuning and RF-pumping, and their transmission lines for probing. Along the edges are six test structures, each containing one SQUID. The reason of the horizontal gap in the middle of the sample is to confine DC currents through the flux lines to their respective resonator. **(b)** A closer look on the SQUID and the pump line design. **(c)** The three capacitors used: the small one is the coupling between the two resonators and the slightly larger ones are the couplings between each resonator and the transmission lines.

an angle $-\alpha$, creating the first electrodes of the Josephson junctions. Then the top parts of the evaporated aluminum is oxidized with a controlled oxygen pressure inside the chamber, thus creating the insulating parts of the Josephson junctions. Last, a second evaporation is done from an angle $+\alpha$, so the new aluminum overlaps the oxidized aluminum, creating the second electrodes of the Josephson junctions.

When a sample is ready, we measure the normal state resistance of the SQUIDs, using six test structures located along the edges of each sample. Fabricating each sample separately allows fine tuning of the normal-state resistance of the junctions, which determines the critical current, and therefore also the Josephson inductance, of the SQUIDs. Hence, after fabricating and measuring one sample, we get feedback on the resistance, which we can use to change the oxidation parameters in the SQUID fabrication process for the next iteration, i.e., if we would like a higher resistance, we increase the oxidation time or the oxygen pressure inside the chamber.

3.3 Cryogenics and measurements

To achieve superconductivity and to observe quantum effects we need to cool down the samples well below 1 K. This is achieved in a dilution refrigerator, which uses a mixture between helium-3 and helium-4 to reach a temperature around 20 mK, where the thermal energy is much less than the excitation energy of our resonators, e.g. $hf/k_B \approx 290$ mK for a frequency of 6 GHz, allowing us to perform measurements unaffected by thermal fluctuations.

In this work we used an Oxford 400 HA wet dilution refrigerator. In this context, wet refers to that the cryostat is submerged into a bath of liquid helium to reach a temperature of 4 K. A pickup tube is then used to withdraw some liquid helium into a pot inside the cryostat, attached to this pot is also a vacuum pump, this will reduce the temperature to 1.5 K. This pot is therefore named the 1K pot. A temperature of 1 K is enough to condense the mixture of helium-3 and helium-4 into their liquid phases, one can then do the same trick and pump on the liquid mixture to reach lower temperatures. Below 0.86 K, there is a phase separation, where the mixture separates into one helium-3 rich part (concentrated phase), and one helium-4 rich part (diluted phase). If helium-3 is transported from the concentrated phase, through the phase boundary, to the diluted phase, cooling will occur, and this is what happens inside the mixing chamber, which is the coldest part of the cryostat. For more details about a dilution refrigerator, and cryostats in general, please see [48].

3.3.1 Measurement setup

An illustration of the measurement setup used in this project is seen in figure 3.3. Both the probe and the pump signals are attenuated on their way down in the cryostat. This serves three purposes: first, it thermally anchors the lines to the different stages of the cryostat, secondly, it puts the signal in the power regime needed, below the level where the resonator is driven non-linear due to the Duffing shift. Finally, it also attenuates the thermal noise generated at the different temperature stages inside the cryostat. The attenuation of the probe lines are 109 dB in total, whereof 59 dB inside the cryostat, and for the pump lines the attenuation is 39 dB, all inside the cryostat. Additionally, there is also some attenuation in all the cables, feedthroughs, and connectors, summing up to roughly 10 dB for each line.

In this work, we mainly measure reflection from one of the input ports, but we cannot just measure at the input port, since the signal would then first get attenuated by 109 dB, and then whatever is reflected would see the same attenuation on its way up again, literally eliminating all signal. Therefore, we use a circulator inside the cryostat to direct the reflected signal to another cable, which is not attenuated. However, this is not enough. The signal is too weak, and it needs to be amplified before we can measure it. This is done in two stages: first, we have a high electron mobility transistor amplifier, with a noise temperature of around 2 K inside the cryostat at the 4 K stage, which we call a low noise amplifier (LNA). At room temperature, we have two cascaded amplifiers to boost the signal even further. If the gain of the LNA is high enough, its noise temperature will determine the total

system noise. The gain of the LNA used here is 35 dB, and the room temperature ones are 23 dB each, yielding a total gain of 91 dB.

The sample is mounted on a printed circuit board (PCB), inside a gold-plated copper box, which is mounted on the mixing chamber of the cryostat, shown in Figure 3.4. The sample box has four SMK-connectors, which are rated from DC to 46 GHz. Two of these are connected to the transmission lines used for probing the resonators, and the other two are connected to the flux lines.

The sample box is surrounded by an aluminum can, also mounted on the mixing chamber, which acts as a shield for magnetic fields. Since aluminum is a superconductor, it will expel all magnetic field from the inside of the can, hence reducing the magnetic flux noise through the SQUIDS on the sample. To provide even more shielding, a mu-metal shield is mounted on the cold plate of the cryostat. The mu-metal will absorb a large part of any low frequency magnetic field penetrating into the cryostat [49].

To change the magnetic flux inside the SQUIDS, there are three possibilities, an external coil, and two on-chip flux lines. The external coil is mounted on the outside of the sample box, which ideally provides a uniform magnetic field density, across the sample. Depending on the number of turns in the coil, the magnetic field produced per current unit can be made rather high, meaning that this is preferable if we want a larger field. However, the trade off is that this field cannot be swept fast.

There are also two individual flux lines on the sample, their purpose is twofold. First, it enables the possibility to change the static magnetic field, locally at each resonator, using a DC current through the flux line. Second, we will use it to modulate the magnetic field fast, also locally at each resonator, using an RF signal. To be able to use both DC and RF on the same flux line, we use a bias-tee, mounted on the connector to the flux line. A bias-tee is a three-terminal device with one DC port, one RF port, and one output port where the two signals are combined.

3.3.2 Measurement techniques

In this project we use two different measurement techniques, first we use a vector network analyzer (VNA) to measure scattering matrices. The scattering matrix of a two terminal device consists of four elements, in our case the reflection at port (A), S_{AA} , the reflection at port (B), S_{BB} , the transmission from (A) to (B), S_{BA} , and the transmission from (B) to (A), S_{AB} . These four parameters are, in general, complex numbers, where the magnitude corresponds to the amount of signal that gets reflected or transmitted, while the phase tells you the amount of phase shift when the signal gets reflected or transmitted. The reflection coefficients can be directly compared with equation (2.10) to find the resonance frequency and the quality factors. Also, the ABCD matrix, equation (2.17), for the two coupled resonators, can be converted directly to an S-matrix.

In the second measurement technique, we use a separate signal generator, and for the measurement we first downconvert the signal, using heterodyne mixing to an IF frequency of 187.5 MHz, which is then sampled with an analog-digital converter (ADC), illustrated in Figure 3.5. This technique is used for measurements done with

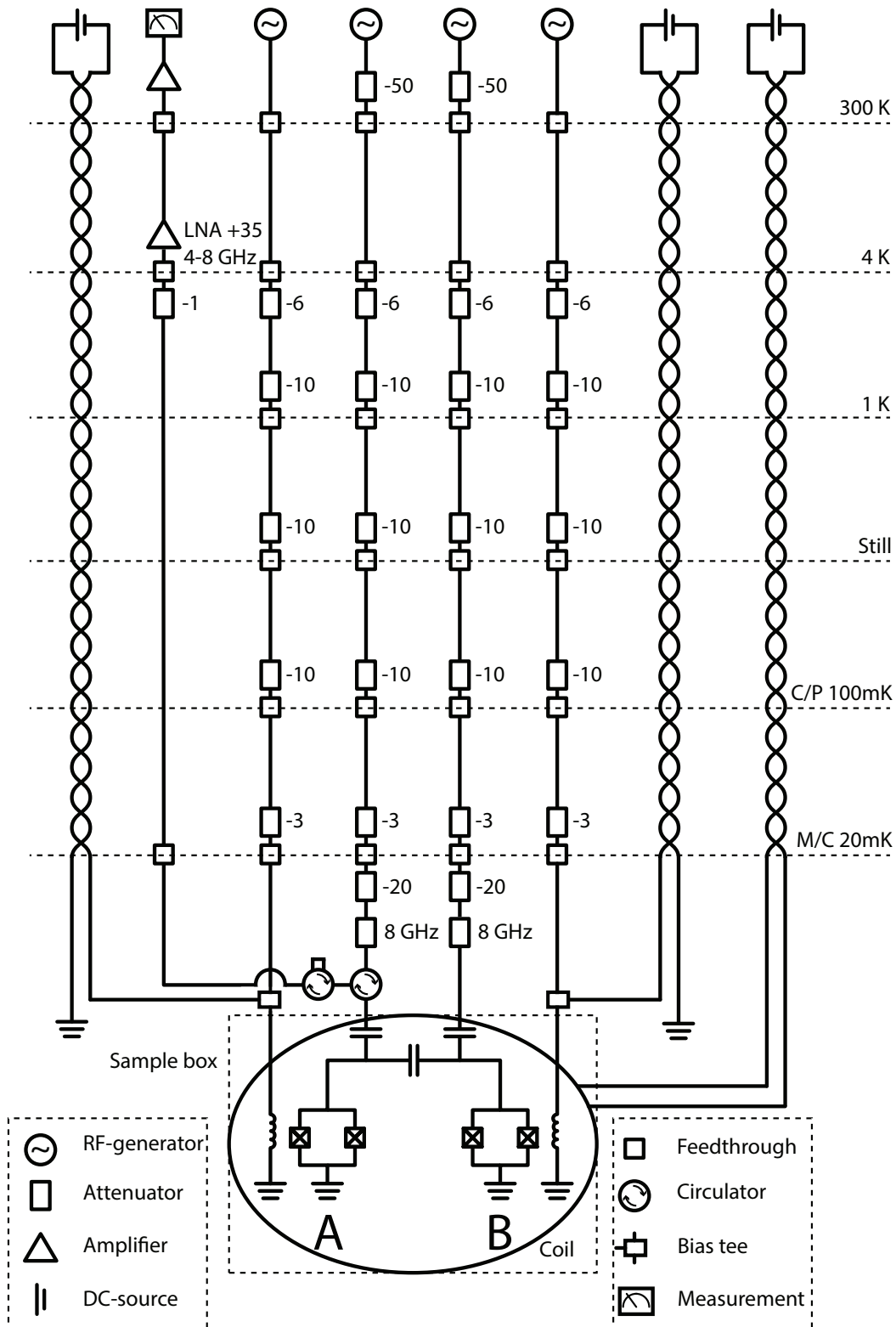


Figure 3.3: Measurement setup used in this project. In this work we refer to the resonator, SQUID and pump line on the left side as (A) and on the other side as (B). The sample is mounted on a PCB inside a gold-plated copper box with four SMK-connectors, two for the input-output ports, and two for the flux lines. On each of the two connectors for the flux lines, a bias-tee is mounted, combining one RF and one DC line.

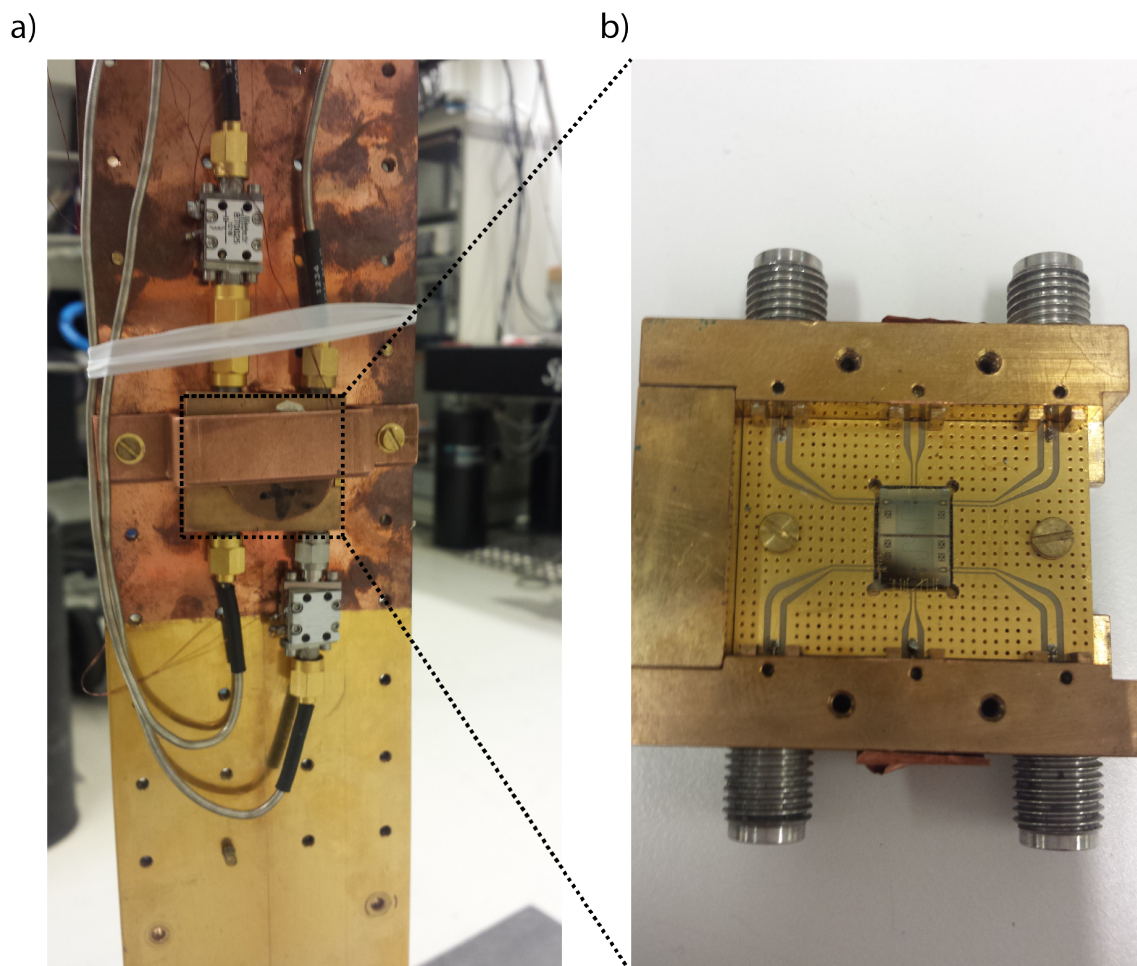


Figure 3.4: Photographs of the sample box, mounted on the tail of the mixing chamber in the dilution refrigerator. **a)** The sample box, together with the external coil, the two bias tees and four coaxial cables. **b)** The open sample box. Inside is a PCB with six CPWs, leading to the wire bonded sample with two coupled resonators.

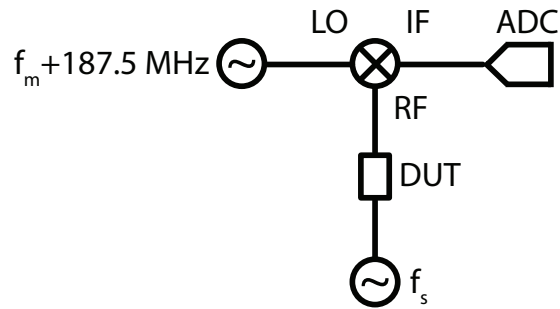


Figure 3.5: The heterodyne detection scheme used in some of the characterizations of the device under test (DUT). Here we use an LO frequency 187.5 MHz above the measurement frequency f_m . Note that we can set f_s and f_m independently of each other.

separate signal frequency, f_s , and measurement frequency, f_m . Another advantage is the fast sampling frequency of the ADC, and the direct access to the raw data in the time domain, allowing for more advanced post-processing of the data than when using a VNA.

4

Results and discussion

THE main part of any project is the results, this is what we have been building up towards with theoretical descriptions and experimental setups. In this chapter, we present first the initial characterization of two coupled resonators. This part is crucial for understanding and explaining the rest of the results. Without proper understanding of the basics, how can you expect to do anything more advanced?

After characterizing the device with all of its components, we move on to the main results of this work, namely the frequency conversion in degenerate and non-degenerate coupled parametric resonators. We have investigated frequency conversion in a few different regimes, as we will explain below. We also try to give interpretations and a physical meaning of the results, when possible. Some of the observations cannot yet be fully explained with a quantitative model. In these cases we will do a bit of reasoning of what the observations could be, but it will require more work to explain them satisfactory.

4.1 Initial characterization

We first characterize the basic properties of the sample with two coupled, tunable, resonators. The properties we are interested in are resonance frequencies, quality factors and circuit parameters. This serves as a verification of our modeling and simulations of the design, and it allows us to further simulate, using the extracted parameters, what results to expect in future experiments.

First, the two coupled resonators are characterized using a vector network analyzer (VNA) to find their resonance frequencies as a function of magnetic flux through the SQUIDs. This is done by varying the current through either the external coil or the individual flux lines. With the VNA, we register both the reflected magnitude and phase as a function of frequency. Ideally, the current through flux line (A) should only affect the flux through SQUID (A), while leaving SQUID (B) unaffected (and *vice versa*), however, this is hard to achieve in reality, leading to unwanted crosstalk.

We characterized the device by measuring the reflection of an incoming signal at port (A), S_{AA} , refer to Figure 4.1 for the naming convention. We were limited to S_{AA} , due to only having one amplifier. While varying the global magnetic flux and measuring S_{AA} , with zero flux offset between the SQUIDs, we obtained the data shown in Figure 4.2 a. A second scan, where we sweep the current through flux line (B), while keeping the current through flux line (A) constant, is shown in Figure 4.2

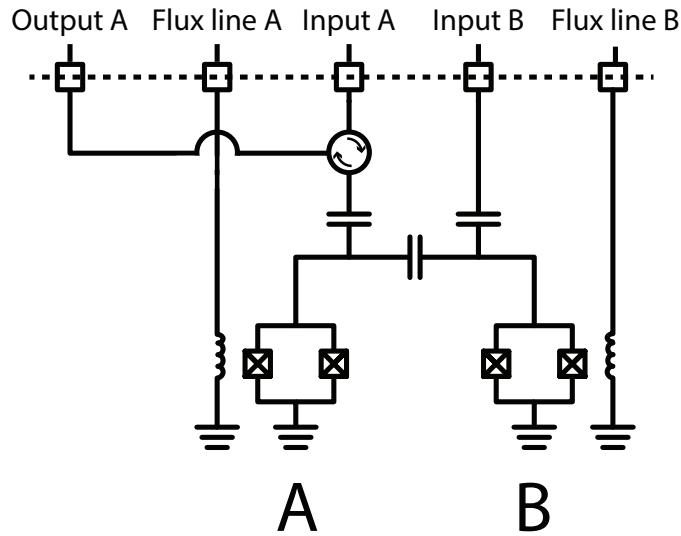


Figure 4.1: A simplified measurement setup, showing the different signal ports, which are referred to throughout this chapter.

b. Through data fitting using equations (2.13), (2.10), and (2.12), we extract the internal and external quality factors, Q_{int} and Q_{ext} , inductive participation ratios γ , and bare resonance frequencies $f_{\lambda/4}$ for both resonators. The fits to both the measurements, are shown in Figure 4.2 c-d, respectively. Additionally, we get the mutual inductance from the flux lines to their respective SQUID, M_F , but, also the crosstalk, $M_{\text{crosstalk}}$. The last thing we extract is the mutual inductance to the external coil, M_C . The external coil couples with very similar strengths to both SQUIDs – the difference is less than 1%, meaning that the magnetic field it produces is uniform across the sample, and that the areas of the SQUIDs are the same.

When the two resonators are tuned to the same frequency, the modes hybridize, and create two new modes. This provides a so called avoided crossing, it looks like the two resonators do not want to cross each other, and instead bend off. This is clearly seen in Figure 4.2 b, at roughly -1 mA. By observing where the avoided crossing between the two resonances is minimum, we can extract the geometric coupling strength $J = 22.95$ MHz between the two resonators. The physical meaning of J is the rate of which the signal is transferred between the two resonators. All the extracted parameters are found in Tables 4.1 and 4.2. We observe that the parameters of the two resonators are very similar, which is to be expected since they are designed to be nominally the same; hence this provides a verification of the reproducibility of our fabrication.

There is however, one issue here. Since we have two ports, (A) and (B), but can only measure at (A) in this experiment, any signal escaping through (B) is lost to us. An offresonant signal is completely reflected at the port, and we do not lose any signal. A signal on resonance, on the other hand, couples into the resonator, and if the two resonators are degenerate, we lose some of the signal into the other resonator, and therefore also out via the other port. Exactly on resonance, and with zero detuning between the two resonators, we lose exactly half the the power,

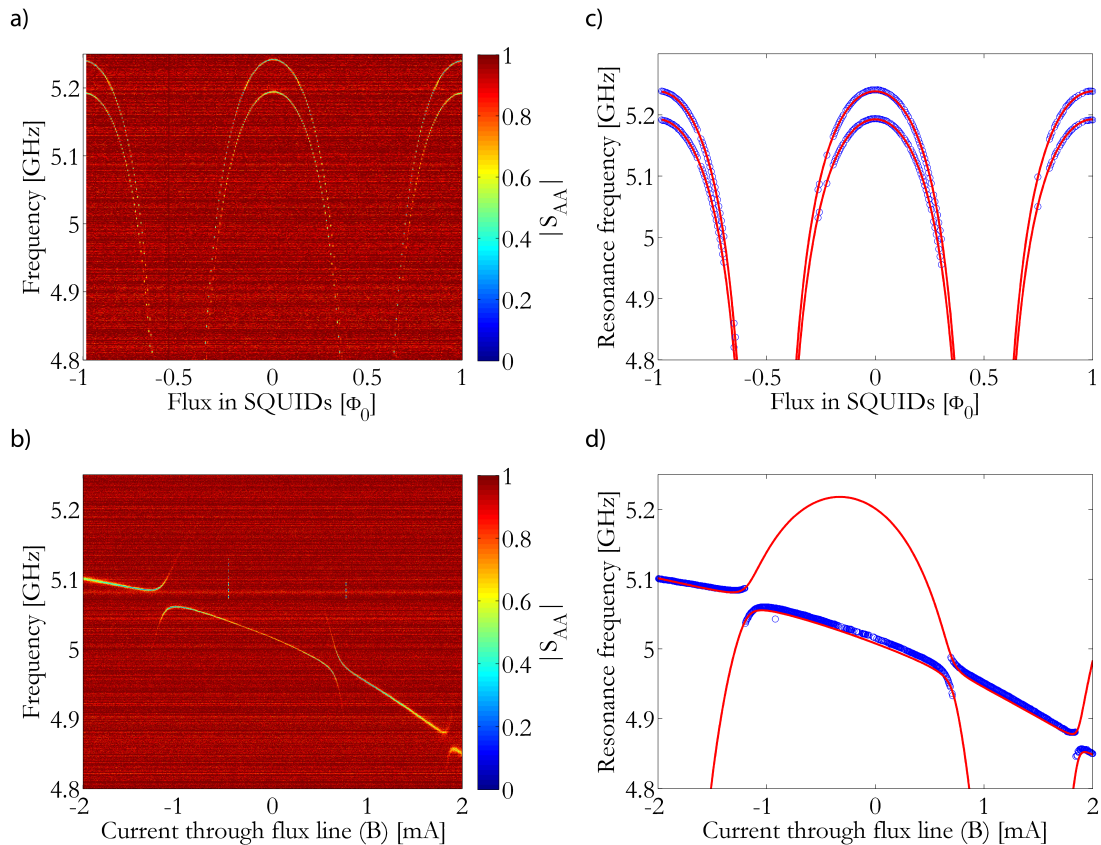


Figure 4.2: Measurements of $|S_{AA}|$ as a function of global and local magnetic fluxes, together with theoretical fits. **(a)** Tuning of both SQUIDs with a global magnetic flux through the external coil, with zero flux offset between (A) and (B). Since there is no flux offset between the two SQUIDs, the distance between the two resonances equals $2J = 46$ MHz. **(b)** Tuning using flux line (B). Note the avoided crossings and also the small crosstalk to the other SQUID. **(c)** and **(d)** Extracted resonance frequencies (blue) from the data in **a** and **b**, together with theoretical fits (red) using equations (2.12) and (2.13). Plotted in **d** is also the predicted frequency of resonator (B) even though we cannot measure it directly.

Table 4.1: Extracted parameters relevant to flux tuning for each of the resonators. The parameters were extracted through data fitting using equations (C.1) and (2.12). The data and the fits are shown in Figure 4.2.

Resonator	γ	$f_{\lambda/4}$ [GHz]	M_F [mA/ Φ_0]	$M_{\text{crosstalk}}$ [mA/ Φ_0]	M_C [μ A/ Φ_0]
A	6.96 %	5.58	35	3	341
B	7.09 %	5.58	35	3	341

Table 4.2: Extracted circuit parameters for resonator (A). The uncertainty for resonator (B) was too large to be able to extract any parameters.

Resonator	C_r	L_r	R_r	C_c	Q_{int}	Q_{ext}
A	0.24 pF	4.17 nH	1.96 M Ω	6.41 fF	14 882	3 742

meaning a factor of $\sqrt{2}$ for the amplitude, assuming identical resonators. This will make the magnitude dips appear deeper as they should be.

This means that, when trying to fit quality factors, where any lost signal will appear as an internal loss, gives a worse estimate of the quality of the resonators. This problem is solved partially by fitting the quality factors for resonator (A) when resonator (B) is detuned. Then no signal will leak out through the port (B). But, since we have no amplifier on port (B), we cannot do the same trick for resonator (B). Instead we will have to fit the two new eigenmodes for the combined system, when the resonators are degenerate, using equation (2.17), already knowing the quality factors of resonator (A). This is a tricky, though, since if there is a slight detuning between the two resonators, this will change the interaction, giving rise to unequal weights of the two modes, which also looks like a change in quality factors. This means that one needs to have a high resolution of the flux tuning to find the bias point with zero detuning, but also in frequency, since one needs quite many points inside the resonance to be able to fit it. All this leads to several millions of data points and is therefore time consuming. Unfortunately, the data we have for this were not good enough, hence the circuit parameters for resonator (B) were not extractable with any accuracy, the uncertainty in the fit was just too large.

4.1.1 Crosstalk - DC and RF

Since it is desirable to operate the individual resonators independently of each other, we need to characterize the crosstalk between the input lines, and from flux line (A) to SQUID (B), and *vice versa*. The DC crosstalk, between the flux lines, can be extracted from the data in Figure 4.2 d. It is done by calculating the ratio of the current necessary to tune the invisible resonator (B) by one flux quantum, compared to that needed to tune the visible resonator (A), by the same amount, using the same flux line. We extract this ratio as 10.7, meaning that if we tune resonator (B) by a certain amount using flux line (B), we will also tune resonator (A) by 9.3% of that amount. Doing this characterization carefully for both flux lines and both SQUIDs, allows us to compensate for the crosstalk using the other flux line. This is done by writing the 2x2 matrix for the mutual inductances, and then diagonalize it.

The RF crosstalk between the two input lines can be measured by applying a

signal on port (A), off resonance, while measuring the outputs of both (A) and (B). Then the signal is applied to port (B) instead, and the measurement is repeated, meaning that we measure the full S-matrix. If there is no crosstalk we expect full reflection, i.e. $|S_{AA}| = |S_{BB}| = 1$ and $|S_{BA}| = |S_{AB}| = 0$, and any deviation from this will tell us the amount of crosstalk. However, since we only have one amplifier in the measurement setup, we first apply a signal at port (A) and measure the output on the same port only, and then switch the input signal to port (B), while maintaining the measurement on port (A). In terms of S parameters this means measurements of $|S_{AA}|$ and $|S_{AB}|$, respectively. Ideally this should give us the same result as the other experiment described first, but due to different attenuation in the lines, *etcetra*, we could have some errors.

We measured this, and conclude an isolation of about 50 dB, meaning that we lose one part out of a hundred thousand to the other input line. If one would need a more exact number, a proper calibration of all the cables and the amplifiers would be needed. However, right now we are only interested in knowing that the crosstalk is low enough, so that it does not cause problems, and even if the error should be as large as 10 dB, an isolation of 40 dB is more than enough.

4.2 Frequency conversion

Here we present the main experimental results of this project. As described earlier, we can operate the device as a beam splitter in several different ways. Either the detuning between the two resonators is very small (degenerate), thus yielding two modes separated by $2J \approx 46$ MHz, or the detuning can be large (non-degenerate), meaning no direct interaction between the two resonators. Furthermore, we can choose the number of pump tones and also which flux lines to use. In this section we will present results in both the degenerate and non-degenerate regimes and using one or two pumps. In all the measurements shown in this section, we measure S_{AA} , and in the cases with two pumps, they are applied at different flux lines. The DC-flux bias point used is close to $\Phi_0/4$, thus yielding a good slope for parametric pumping. This bias point corresponds to resonance frequencies around 5.1 GHz, but you will see that they change a bit between different experiments, due to some instabilities in the magnetic flux inside the cryostat.

4.2.1 Degenerate case

With zero or very small detunings between the resonators, such that $|f_A - f_B| \ll \Gamma_{A,B}$, where $\Gamma_{A,B}$ are the linewidths of the resonators, we introduce a direct interaction between them, and the system hybridizes into two new eigenmodes, separated by $2J \approx 46$ MHz, shown in Figure 4.2. As in previous chapters, we call the higher of these two new modes f_1 and the lower one f_2 . We call this the degenerate regime, and here the two resonators are a combined system, meaning that the eigenmodes are not localized to one resonator, instead they are spread out over both resonators. This was described in section C, where we derived the electric field amplitude as a function of position in the resonator. This means that it should not matter if we apply the pump tone to SQUID (A) or (B), since the system is symmetric around

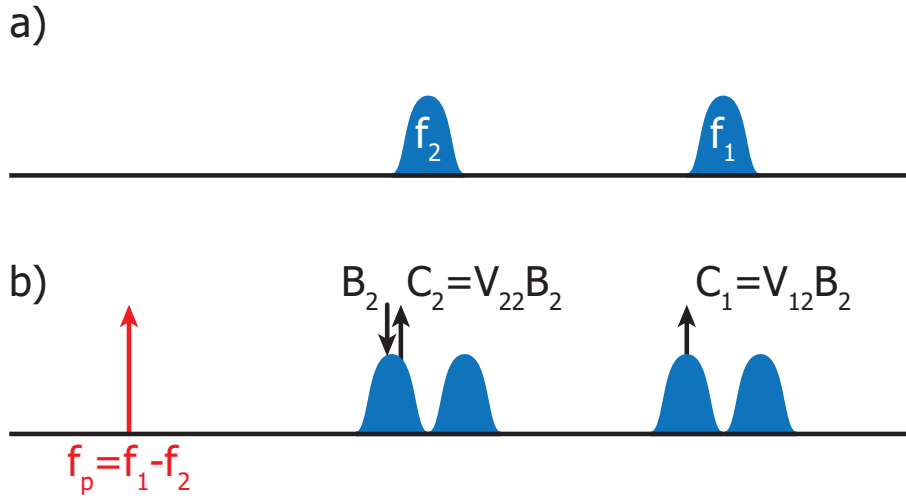


Figure 4.3: Pump scheme used for measuring frequency conversion. (a) The two eigenmodes of the system in the absence of a parametric pump. (b) By turning on a pump at the difference frequency, the modes couple together and hybridize into four new modes. By applying a signal B_2 close to f_2 we can measure what gets reflected, given by $V_{22}B_2$, and what gets converted, $V_{12}B_2$. The two matrix elements are given by equations (2.37) and (2.39), respectively.

the coupling capacitor and both SQUIDs acts as a boundary condition for both the modes, since they are spread out over both resonators, shown in Figure 2.6. We first consider the simplest case of just one pump signal; the result is then described by the theory in section 2.2.4, and mainly by equations (2.37)- (2.40).

Using one pump

By using one pump tone with a frequency $f_p = 2J$ (the distance between the two resonances f_1 and f_2), we achieve frequency conversion (or beam splitting) between these two modes. This is depicted in Figure 4.4, where the pump is applied to SQUID (A) with a power of -10 dBm at the generator, and the pump frequency f_p is swept close to $2J$. First, when the pump frequency is far detuned from $2J$, the two modes are left intact. As it gets closer, each mode starts to split up again, generating two new avoided crossings with an invisible mode, shown in Figure 4.3. There is now a direct interaction between f_1 and f_2 , similar to the one between the two resonators. However, this new interaction is supplied by the parametric pump, and, as we shall see, it is also tunable in coupling strength. Then, when the pump frequency gets higher, the system returns to the two original modes.

We then repeated the same experiment, but instead we applied the pump signal to SQUID (B). This gave the same results as the previous experiment, as expected for two identical resonators, since the system is then symmetric around the coupling capacitor.

Next, we investigate the observed splitting at zero pump detuning, as a function of pump power P_p . From equation (2.37) it follows that the minimum splitting observed in Figure 4.4, assuming no internal losses, is equal to 2ϵ , i.e. twice the effective pump strength, which is proportional to the pump amplitude (not the

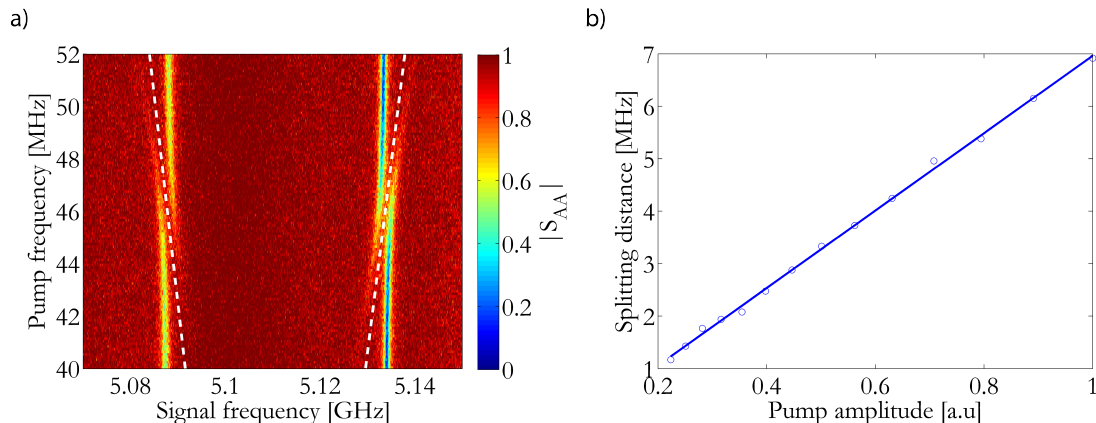


Figure 4.4: Beam splitting in the degenerate case, using one pump tone on SQUID A. **(a)** Depicted is the measurement of $|S_{AA}|$, as a function of pump frequency f_p , at a power of $P_p = -8$ dBm at the generator. The white, dashed, lines, illustrates the invisible mode that couples to the original modes, hence creating the avoided crossings. **(b)** Pump amplitude dependence of the splitting distance between the two new modes, using a parametric pump at $f_p = f_1 - f_2$. The observed splitting is clearly linearly dependent on the pump amplitude, as expected from theory.

power). In Figure 4.4 **b**, we plot the splitting distance as a function of pump amplitude and a linear dependence is clearly observed, as expected from theory. This means, in analogue with the capacitive coupling strength J between the resonators, that the coupling strength between mode f_1 and f_2 is ϵ , and that it is tunable with pump power. ϵ can also be interpreted as the rate of which the signal is converted between the two modes. One could also imagine situations where the pump signal is turned off and on, hence temporally removing the coupling completely. This is not possible for the capacitive coupling, since the capacitor is always there and at a constant value. However, the coupling between (A) and (B) can be turned off by detuning them from each other, but this also means that their frequencies change, which could be a problem in a larger system, where there are other components with similar frequency close by, to which we do not want to couple. If everything is stationary in frequency, as in the parametric coupling, it is easier to avoid any undesired couplings.

The measurements shown in figure 4.4, and discussed above, provides suggest that we achieved frequency conversion, but all we have seen so far is a splitting of the eigenmodes. In order to verify that we achieve frequency conversion, we do a second measurement of the actual conversion. To measure the conversion from one frequency to another, i.e. the V_{12} and V_{21} elements from equations (2.38) and (2.40), we need to send in a signal at one mode, and measure at the other, e.g. $f_s = f_2$, and $f_m = f_1$. If there is frequency conversion from f_2 to f_1 , we should measure some signal at f_1 , even though we do not apply any signal at that frequency. For these measurements we use the heterodyne detection scheme illustrated in Figure 3.5, instead of the VNA. This allows us to set the signal frequency, and the measurement frequency, independent of each other. But since we also can set the frequencies to be identical, this allows us to measure the full \hat{V} matrix. However, changing

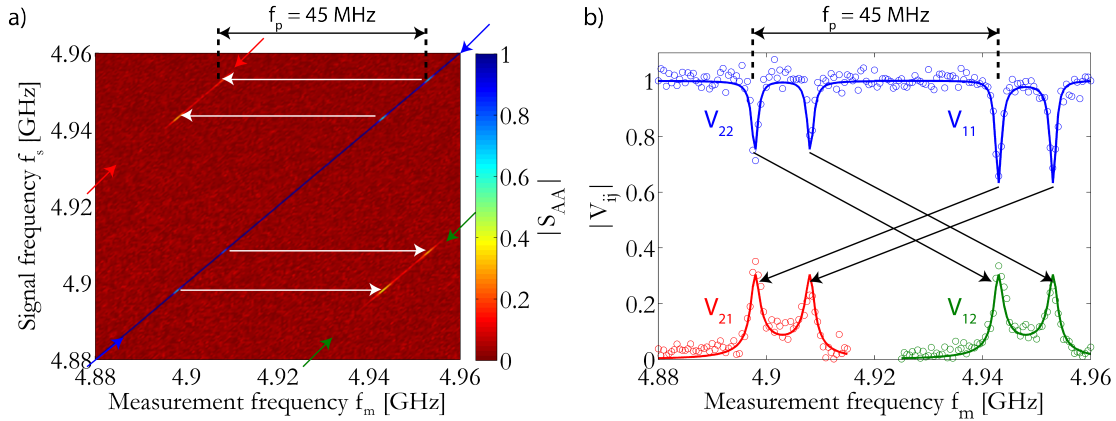


Figure 4.5: Frequency conversion using one parametric pump in two degenerate $\lambda/4$ resonators. **(a)** Reflected magnitude $|S_{AA}|$ as a function of signal and measurement frequencies. Away from resonance, all of the applied signal is reflected back at the signal frequency, but on resonance some parts gets reflected at $f_s \pm f_p$, illustrated by the white arrows. **(b)** Three linecuts of **a**, indicated by arrows in corresponding colors. The four pairs of resonance are measurements of the magnitude of the four input-output matrix elements in equations (2.37)-(2.40), and the solid lines are fits using these equations. Blue is V_{11} and V_{22} , while green is V_{12} , and red is V_{21} . The black arrows corresponds to how the signals are converted.

either the signal frequency, f_s , or the measurement frequency, f_m , removes the phase information, since for each new frequency, the signal gets a random phase, making it impossible to compare how the phase response varies with frequency. This means that we can only measure the magnitude of the matrix elements using this method. Also this method is slower than using the VNA, meaning that the parameter space (signal, measurement, and pump frequencies, together with pump power) measurable in a reasonable amount of time is limited. The result of this measurement is depicted in Figure 4.5 **a**. This gives us direct evidence that it is in fact frequency conversion that we observe.

One might say that the conversion efficiency is not so high, only 30% of the incoming signal is converted. However, we need to take into account the problem of signal leaking out through port (B). With access to that information, the peaks in V_{12} and V_{21} should be multiplied by a factor $\sqrt{2}$, meaning a real conversion efficiency of 50%, limited by the internal losses of the resonators.

Using two pumps - phase dependence

One might ask, what happens if we introduce a pump signal on SQUID (B) as well? To answer this, let's first consider the case when both pumps are identical in frequency and power. The only degree of freedom left is the phase difference between the two signals. Figure 4.6 **a** shows beam splitting as a function of phase difference between the pump signals. We can clearly see regions of enhanced splitting, but also regions of almost complete elimination of the splitting. These specific phase differences correspond to a breathing mode and a translation mode, respectively. We can fit this with a simple modification to the input-output matrix: in equations

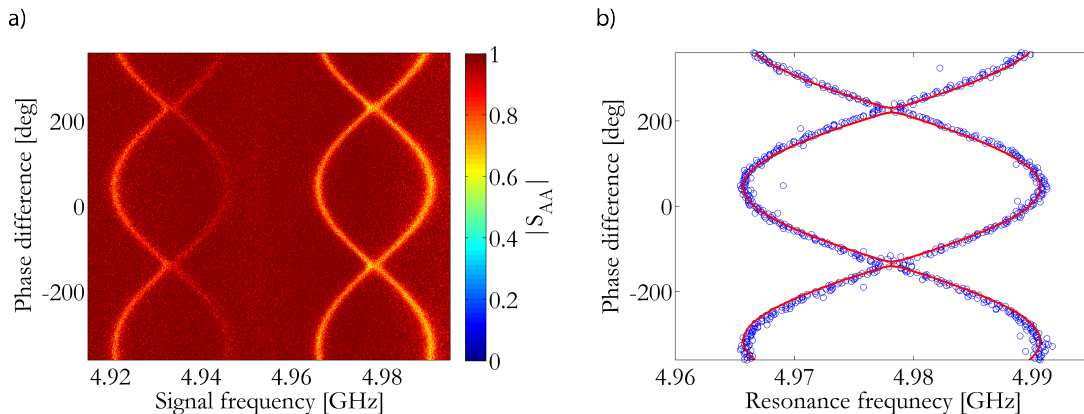


Figure 4.6: Beam splitting using two degenerate pump tones, sweeping the phase offset between the two pump signals. Note that zero phase difference is set arbitrarily and has no physical meaning. **(a)** Experimental data, the two pump tones are set to identical frequencies $f_p = 45$ MHz and pump powers $P_p = -1$ dBm at the generators. **(b)** Fit of the peak separation as a function of the phase difference θ where blue is the data and red the fit with $\epsilon' = 12.5$ MHz.

(2.37)-(2.40) we introduce an effective pumping strength $\epsilon = \epsilon' \sin(\theta/2)$, where ϵ' is the pumping strength in absence of the second pump and θ is the phase angle between the two pumps. The fit is shown in Figure 4.6 **b** and the extracted effective pump strength is $\epsilon' = 12.5$ MHz. There is some discrepancy between the frequency of the oscillations in the fit and the data, which could be due to a frequency offset between the two pump signals, hence giving rise to a time-varying phase difference.

Using two pumps - multi mode

In this case we also use two pump tones, one on each SQUID, but we remove the constraint of same frequency and pump power. Due to different frequencies, the phase dependence also vanishes. First we lock one pump signal, at SQUID (A), to the difference frequency between the two modes, and then we sweep the frequency of the pump at (B). The first pump splits the two original modes into four, and when the second pump's frequency matches the distance between two or more modes, we get further splittings. The result of this experiment is depicted in Figure 4.7.

4.2.2 Non-degenerate case

Another point of operation is when the two resonators are separated in frequency. This turns off the direct interaction between the resonators and we are left with two individual systems, i.e., the modes are localized in each resonator. This means, for example, that all signal sent into resonator (A) will stay there or leak out through port (A) again. However, we can introduce an interaction just as before by pumping on the difference frequency between the two resonators ($f_p = |f_A - f_B|$). There is, however, one major difference to be pointed out here: in the previous experiment it did not matter which SQUID we pumped, since both were identical and acted as a boundary condition for both modes. Now, in the non-degenerate mode, SQUID

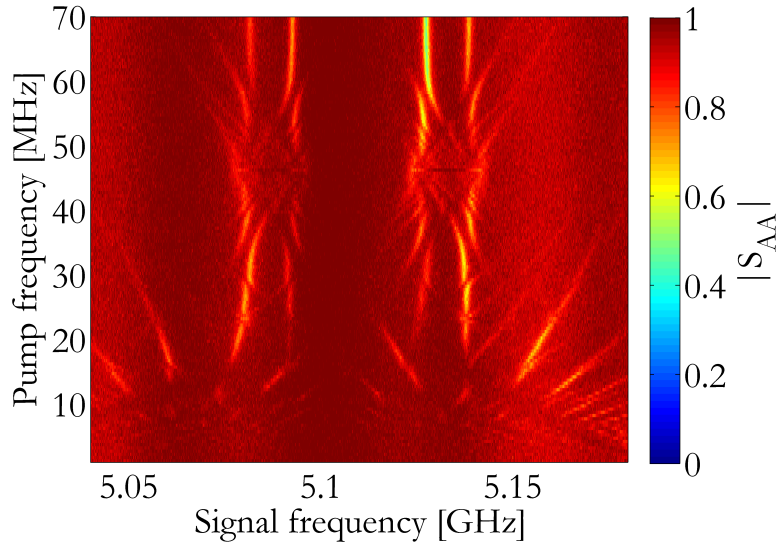


Figure 4.7: Beam splitting using two pump tones. The pump on SQUID (A) is locked at 46 MHz and a power of 6 dBm at the generator, whereas the pump on SQUID (B) is swept in frequency, while maintaining a power of 2 dBm at the generator.

(A) is only a boundary condition for resonator (A) and *vice versa*. This should mean that if we send in a signal, resonant with (A), on port (A), while pumping SQUID (A) we can get conversion into resonator (B); however, if we send a signal on another frequency and port combination, e.g. a signal on port (B) while still pumping SQUID (A), or a signal on (A) and instead pump on SQUID (B), we will not achieve frequency conversion.

This implies that we can shuttle photons from resonator (A) to (B), while blocking the other way around, creating an isolator for microwaves. However, this isolator also changes the frequency of the signal, which could be an undesirable effect of an isolator. In Figure 4.8 **a**, we see such an experiment where we measure S_{AA} when a pump signal is applied to (A) at $f_p = |f_A - f_B|$. We can see the same behaviour as before with the avoided crossing and two new eigenmodes. If we then switch to pumping SQUID (B) with the same frequency and amplitude, but still measure S_{AA} we see in Figure 4.8 **b** that the effect is heavily reduced and it is not possible to resolve the two modes anymore. The fact that we can still see some tendencies of an avoided crossing could be explained by crosstalk from flux line (B) to SQUID (A) and will need further investigations.

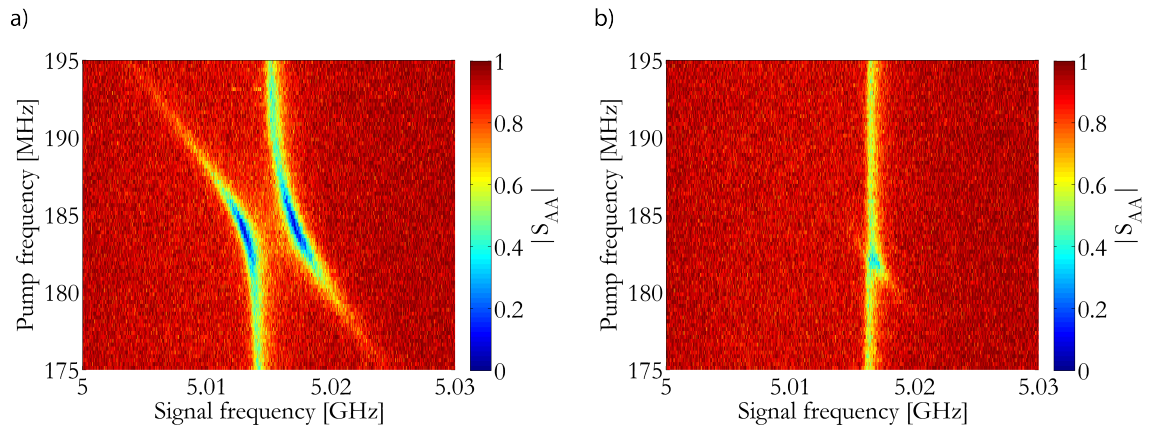


Figure 4.8: Beam splitting in the non-degenerate case. In both figures we measure $|S_{AA}|$ as a function of pump frequency and with a constant pump power $P_p = 6$ dBm at the generator. **(a)** Here the pump signal is applied at SQUID (A) and for **(b)** it is applied at SQUID (B).

5

Conclusions and outlooks

IN this work we have gone from a theoretical description of a parametric frequency converter in the microwave regime, to a fully functioning device. The device consisted of two coupled superconducting resonators, which were tunable to allow for parametric modulation. We have shown how to simulate, fabricate and measure such a device. It was designed to have low cross talk between both RF-ports, and DC flux lines. The coupling strengths were designed to be reasonable for a proof of concept. All of these criteria were met in the experiment. The DC-crosstalk between the two flux-tuning lines was measured to be 9.3%; this might seem quite high, but we can compensate for it using the two flux lines, giving us full control of the individual frequencies of the resonators. The RF-crosstalk between port (A) and (B) was measured to 50 dB, making it negligible.

Next, the parametric frequency conversion itself was performed. It was done with a few different parametric modulation schemes: with the resonators degenerate and non-degenerate, with one and two pump signals, and finally, with and without phase dependence of two pump signals. In the case of degeneracy and one pump signal, we reached a frequency conversion efficiency of 50%.

A few improvements and measurements should be carried out in future work. First, an amplifier should be installed on the probe line for resonator (B), so that all the S-parameters can be obtained simultaneously, allowing us to extract the parameters of resonator (B) with higher accuracy. With a second amplifier we would also be able to measure and verify the isolation in the non-degenerate case, meaning that light is only converted one way. One would need to show that $|S_{AA}| = |S_{AB}| = 0$ and $|S_{BB}| = |S_{BA}| = 1$.

To build a device with higher frequency conversion efficiency, one would need to decrease either the internal loss rates, Γ_i , or increase the external couplings, Γ_0 , since the ratio of these two sets the efficiency. Increasing the external coupling rate is straightforward, just by making the coupling capacitance to the probe lines, C_{out} , higher. However, we need to make sure that the coupling between the two resonators, J , is still much larger than Γ_0 . Decreasing Γ_i is more difficult, since it is set by how well we can fabricate the resonators and the SQUIDs.

A good and natural next step would be to repeat the experiment done by Zakka-Bajjani *et al.* [15], where they show one photon in a superposition of two different colors, or frequencies. The challenge in this experiment is to first create a single photon, and then to measure the state of this single photon. In their experiment, they used a superconducting qubit to first generate a single-photon Fock state, which can then be coherently transferred between the two modes by turning on the pump for a certain amount of time. The qubit is then used as a probe by tuning it into

resonance with one of the modes, absorbing the single photon (if it is there) and then reading out the state of the qubit out using the standard technique of dispersive readout[6, 33]. If the measurement shows that the qubit was in its excited state, it follows that the photon must have been in that mode as well.

To implement this experiment in the device presented in this work, one would need to add at least one qubit to the system. For symmetry purposes one could think of adding a qubit to each resonator, enabling measurements of the spatial location of the photon. Every qubit would also need individual flux-tuning lines to enable fast control of their transition frequencies, hence increasing the complexity of the design.

If, in the non-degenerate case, we can show that photons are only converted one way, e.g. from port (A) to port (B), but not *vice versa*, it should be possible, in a pulsed pump scheme, not only to put the photon in a superposition of two frequencies, but also in a superposition of spatial locations. A pumping scheme similar to the one used in [15] would be utilized to study the coherent transfer of photons, not only in frequency but also in space.

Bibliography

- [1] E. Carlsson and S. Gevorgian, “Conformal mapping of the field and charge distributions in multilayered substrate cpws,” *Microwave Theory and Techniques, IEEE Transactions on*, vol. 47, no. 8, pp. 1544–1552, 1999.
- [2] M. Planck, “Ueber das gesetz der energieverteilung im normalspectrum,” *Annalen der physik*, vol. 309, no. 3, pp. 553–563, 1901.
- [3] A. Einstein, “Über einen die erzeugung und verwandlung des lichtetes betreffenden heuristischen gesichtspunkt,” *Annalen der Physik*, vol. 322, no. 6, pp. 132–148, 1905.
- [4] D. F. Walls and G. J. Milburn, *Quantum optics*. Springer Science & Business Media, 2007.
- [5] Y. Nakamura, Y. A. Pashkin, and J. Tsai, “Coherent control of macroscopic quantum states in a single-cooper-pair box,” *Nature*, vol. 398, no. 6730, pp. 786–788, 1999.
- [6] A. Wallraff, D. I. Schuster, A. Blais, L. Frunzio, R.-S. Huang, J. Majer, S. Kumar, S. M. Girvin, and R. J. Schoelkopf, “Strong coupling of a single photon to a superconducting qubit using circuit quantum electrodynamics,” *Nature*, vol. 431, no. 7005, pp. 162–167, 2004.
- [7] J. Majer, J. Chow, J. Gambetta, J. Koch, B. Johnson, J. Schreier, L. Frunzio, D. Schuster, A. Houck, A. Wallraff, *et al.*, “Coupling superconducting qubits via a cavity bus,” *Nature*, vol. 449, no. 7161, pp. 443–447, 2007.
- [8] D. P. DiVincenzo, “Quantum computation,” *Science*, vol. 270, no. 5234, pp. 255–261, 1995.
- [9] C. H. Bennett and D. P. DiVincenzo, “Quantum information and computation,” *Nature*, vol. 404, no. 6775, pp. 247–255, 2000.
- [10] M. V. Gustafsson, T. Aref, A. F. Kockum, M. K. Ekström, G. Johansson, and P. Delsing, “Propagating phonons coupled to an artificial atom,” *Science*, vol. 346, no. 6206, pp. 207–211, 2014.
- [11] J. Koch, M. Y. Terri, J. Gambetta, A. A. Houck, D. Schuster, J. Majer, A. Blais, M. H. Devoret, S. M. Girvin, and R. J. Schoelkopf, “Charge-insensitive qubit design derived from the cooper pair box,” *Physical Review A*, vol. 76, no. 4, p. 042319, 2007.

- [12] D. Loss and D. P. DiVincenzo, “Quantum computation with quantum dots,” *Physical Review A*, vol. 57, no. 1, p. 120, 1998.
- [13] F. Jelezko and J. Wrachtrup, “Single defect centres in diamond: A review,” *physica status solidi (a)*, vol. 203, no. 13, pp. 3207–3225, 2006.
- [14] T. H. Johnson, S. R. Clark, and D. Jaksch, “What is a quantum simulator?,” *EPJ Quantum Technology*, vol. 1, no. 1, pp. 1–12, 2014.
- [15] E. Zakka-Bajjani, F. Nguyen, M. Lee, L. R. Vale, R. W. Simmonds, and J. Aumentado, “Quantum superposition of a single microwave photon in two different colour states,” *Nature Physics*, vol. 7, no. 8, pp. 599–603, 2011.
- [16] M. Tinkham, *Introduction to superconductivity*. Courier Corporation, 2012.
- [17] D. M. Pozar, *Microwave engineering*. John Wiley & Sons, 2009.
- [18] H. K. Onnes, “The resistance of pure mercury at helium temperatures,” *Commun. Phys. Lab. Univ. Leiden*, vol. 12, no. 120, p. 1, 1911.
- [19] W. Meissner and R. Ochsenfeld, “Ein neuer effekt bei eintritt der supraleitfähigkeit,” *Naturwissenschaften*, vol. 21, no. 44, pp. 787–788, 1933.
- [20] J. Bardeen, L. N. Cooper, and J. R. Schrieffer, “Theory of superconductivity,” *Phys. Rev.*, vol. 108, pp. 1175–1204, Dec 1957.
- [21] B. D. Josephson, “Possible new effects in superconductive tunnelling,” *Physics Letters*, vol. 1, no. 7, pp. 251–253, 1962.
- [22] P. Anderson and J. Rowell, “Probable observation of the josephson superconducting tunneling effect,” *Physical Review Letters*, vol. 10, no. 6, pp. 230–232, 1963.
- [23] R. P. Feynman, R. B. Leighton, and M. Sands, *The feynman lectures on physics. 3: Quantum mechanics: Lectures on physics*. Addison-Wesley, 1965.
- [24] S. Levy, E. Lahoud, I. Shomroni, and J. Steinhauer, “The ac and dc josephson effects in a bose–einstein condensate,” *Nature*, vol. 449, no. 7162, pp. 579–583, 2007.
- [25] P. Richards and P. Anderson, “Observation of the analog of the ac josephson effect in superfluid helium,” *Physical Review Letters*, vol. 14, no. 14, p. 540, 1965.
- [26] M. H. Anderson, J. R. Ensher, M. R. Matthews, C. E. Wieman, and E. A. Cornell, “Observation of bose–einstein condensation in a dilute atomic vapor,” *Science*, vol. 269, no. 5221, pp. 198–201, 1995.
- [27] M. Abbarchi, A. Amo, V. Sala, D. Solnyshkov, H. Flayac, L. Ferrier, I. Sagnes, E. Galopin, A. Lemaître, G. Malpuech, *et al.*, “Macroscopic quantum self-trapping and josephson oscillations of exciton polaritons,” *Nature Physics*, vol. 9, no. 5, pp. 275–279, 2013.

-
- [28] R. Jaklevic, J. Lambe, A. Silver, and J. Mercereau, “Quantum interference effects in josephson tunneling,” *Physical Review Letters*, vol. 12, no. 7, p. 159, 1964.
- [29] J. Clarke and A. I. Braginski, *The SQUID handbook*. Wiley Online Library, 2006.
- [30] M. Devoret and R. Schoelkopf, “Superconducting circuits for quantum information: an outlook,” *Science*, vol. 339, no. 6124, pp. 1169–1174, 2013.
- [31] Y. Yin, Y. Chen, D. Sank, P. O’Malley, T. White, R. Barends, J. Kelly, E. Lucero, M. Mariantoni, A. Megrant, *et al.*, “Catch and release of microwave photon states,” *Physical review letters*, vol. 110, no. 10, p. 107001, 2013.
- [32] M. Pierre, I.-M. Svensson, S. R. Sathyamoorthy, G. Johansson, and P. Delsing, “Storage and on-demand release of microwaves using superconducting resonators with tunable coupling,” *Applied Physics Letters*, vol. 104, no. 23, p. 232604, 2014.
- [33] A. Blais, R.-S. Huang, A. Wallraff, S. Girvin, and R. J. Schoelkopf, “Cavity quantum electrodynamics for superconducting electrical circuits: An architecture for quantum computation,” *Physical Review A*, vol. 69, no. 6, p. 062320, 2004.
- [34] B. Yurke, L. Corruccini, P. Kaminsky, L. Rupp, A. Smith, A. Silver, R. Simon, and E. Whittaker, “Observation of parametric amplification and deamplification in a josephson parametric amplifier,” *Physical Review A*, vol. 39, no. 5, p. 2519, 1989.
- [35] C. P. Wen, “Coplanar waveguide: A surface strip transmission line suitable for nonreciprocal gyromagnetic device applications,” *Microwave Theory and Techniques, IEEE Transactions on*, vol. 17, no. 12, pp. 1087–1090, 1969.
- [36] M. Wallquist, V. Shumeiko, and G. Wendin, “Selective coupling of superconducting charge qubits mediated by a tunable stripline cavity,” *Physical Review B*, vol. 74, no. 22, p. 224506, 2006.
- [37] M. Sandberg, C. Wilson, F. Persson, T. Bauch, G. Johansson, V. Shumeiko, T. Duty, and P. Delsing, “Tuning the field in a microwave resonator faster than the photon lifetime,” *Applied Physics Letters*, vol. 92, no. 20, p. 203501, 2008.
- [38] M. Dykman, C. Maloney, V. Smelyanskiy, and M. Silverstein, “Fluctuational phase-flip transitions in parametrically driven oscillators,” *Physical Review E*, vol. 57, no. 5, p. 5202, 1998.
- [39] P. Krantz, Y. Reshitnyk, W. Wustmann, J. Bylander, S. Gustavsson, W. D. Oliver, T. Duty, V. Shumeiko, and P. Delsing, “Investigation of nonlinear effects in josephson parametric oscillators used in circuit quantum electrodynamics,” *New Journal of Physics*, vol. 15, no. 10, p. 105002, 2013.

- [40] W. Wustmann and V. Shumeiko, “Parametric resonance in tunable superconducting cavities,” *Physical Review B*, vol. 87, no. 18, p. 184501, 2013.
- [41] V. Shumeiko, “Two coupled $\lambda/4$ resonators,” *Unpublished*, 2015.
- [42] B. Yurke and J. S. Denker, “Quantum network theory,” *Physical Review A*, vol. 29, no. 3, p. 1419, 1984.
- [43] C. Wilson, T. Duty, and P. Delsing, “Fluctuating nonlinear oscillators: from nanomechanics to quantum superconducting circuits,” Oxford University Press, 2012.
- [44] C. Wilson, T. Duty, M. Sandberg, F. Persson, V. Shumeiko, and P. Delsing, “Photon generation in an electromagnetic cavity with a time-dependent boundary,” *Physical review letters*, vol. 105, no. 23, p. 233907, 2010.
- [45] P. Krantz, “Parametrically pumped superconducting circuits,” 2013.
- [46] M. Simoen, C. Chang, P. Krantz, J. Bylander, P. Delsing, and C. Wilson, “Characterization of a multimode coplanar waveguide parametric amplifier,” *arXiv preprint arXiv:1409.8160*, 2014.
- [47] G. Dolan, “Offset masks for lift-off photoprocessing,” *Applied Physics Letters*, vol. 31, no. 5, pp. 337–339, 1977.
- [48] O. V. Lounasmaa, *Experimental principles and methods below 1 K*, vol. 8. Academic Press London, 1974.
- [49] D. C. Jiles, *Introduction to magnetism and magnetic materials*. CRC press, 1998.

A

Clean room processes

- Cleaning of substrate
 - 1165 Remover at 70°C for 5 min
 - IPA bath, circulation for 2 min
 - Rinse in water
 - Blow dry with N₂
 - Strip in oxygen plasma, 250W for 1 min
- Sputtering of Nb
 - Annealing at 1200°C overnight, ramp 5°C per min
 - Sputtering of Nb
- Contact pads and alignment marks
 - 1165 Remover at 70°C for 5 min
 - Rinse in IPA
 - Blow dry with N₂
 - Ash in oxygen plasma, 50W for 20 sec
 - Pre-bake at 110°C for 1 min
 - Spin LOR3B at 3000 rpm for 1 min
 - Soft-bake at 200°C for 5 min
 - Spin S1813 at 3000 rpm for 1 min
 - Soft-bake at 110°C for 2 min
 - Expose for 8.5 sec using low-vac mode
 - Develop using MF319 for 50 sec
 - Ash in oxygen plasma, 50W for 20 sec
 - Evaporation of 3 nm of Ti, 80 nm of Au and 10 nm of Pd
- Resonator and transmission lines
 - 1165 Remover at 70°C for 5 min
 - Rinse in IPA

- Blow dry with N₂
- Ash in oxygen plasma, 50W for 20 sec
- Pre-bake at 130°C for 1 min
- Spin UV60 at 3000 rpm for 1 min
- Soft-bake at 130°C for 1 min
- Expose with 70 nA with a dose of 27 $\mu\text{C}/\text{mm}^2$
- Develop using MF319 for 50 sec
- Ash in oxygen plasma, 50W for 20 sec
- Etching using NF₃
- SQUIDS
 - 1165 Remover at 70°C for 5 min
 - Rinse in IPA
 - Blow dry with N₂
 - Ash in oxygen plasma, 50W for 20 sec
 - Pre-bake at 170°C for 1 min
 - Spin MMA(8.5)EL10 500 rpm for 5 sec, 2000 rpm for 45 sec
 - Soft-bake at 170°C for 5 min
 - Spin ARP 3200.09 2:1 3000 rpm for 1 min
 - Soft-bake at 170°C for 5 min
 - Expose with 2 nA with a dose of 280 $\mu\text{C}/\text{mm}^2$
 - Dice into 24 samples
 - Develop top layer using n-Amylacetate for 2 min
 - Develop bottom layer using H₂O:IPA 1:4 for 7 min
 - Ash in oxygen plasma, 50W for 20 sec
 - Evaporate 40 nm aluminum from 25°
 - Oxidize with a pressure of 0.2 mBar for 30 min
 - Evaporate 65 nm aluminum from –25°

B

Derivation of the Josephson-relations

We start out by writing two coupled Schrödinger equations for two superconductors separated by an insulating layer, assuming a constant coupling K between the two superconductors

$$\begin{aligned}i\hbar\frac{\partial\psi_1}{\partial t} &= U_1\psi_1 + K\psi_2 \\i\hbar\frac{\partial\psi_2}{\partial t} &= U_2\psi_2 + K\psi_1\end{aligned}\tag{B.1}$$

where ψ_1 and ψ_2 represents the wavefunctions in each superconductor and U_1 , U_2 are the energies of the lowest energy states on respective side of the insulating layer. If there are no coupling ($K = 0$) we would just have two equations describing the lowest energy state in each of the superconductors, the coupling introduces a leakage from one side to the other.

Since the Cooper-pairs in a superconductor forms a Bose-Einstein condensate we can describe the Cooper-pairs with a single wavefunction, constant in space if we assume the London gauge: $\psi_1 = \sqrt{\rho_1}e^{i\theta_1}$, where ρ_1 is the density of Cooper-pairs and θ_1 their phase. If we plug this into equation (B.1) we get:

$$\begin{aligned}i\hbar\left(\frac{1}{2}\frac{\dot{\rho}_1}{\sqrt{\rho_1}} + i\sqrt{\rho_1}\dot{\theta}_1\right)e^{i\theta_1} &= U_1\sqrt{\rho_1}e^{i\theta_1} + K\sqrt{\rho_2}e^{i\theta_2} \\i\hbar\left(\frac{1}{2}\frac{\dot{\rho}_2}{\sqrt{\rho_2}} + i\sqrt{\rho_2}\dot{\theta}_2\right)e^{i\theta_2} &= U_2\sqrt{\rho_2}e^{i\theta_2} + K\sqrt{\rho_1}e^{i\theta_1}\end{aligned}\tag{B.2}$$

Next multiply the first equation with ψ_1^* and the second one with ψ_2^* , yielding:

$$\begin{aligned}i\hbar\left(\frac{1}{2}\dot{\rho}_1 + i\rho_1\dot{\theta}_1\right) &= U_1\rho_1 + K\sqrt{\rho_1\rho_2}e^{i(\theta_2-\theta_1)} \\i\hbar\left(\frac{1}{2}\dot{\rho}_2 + i\rho_2\dot{\theta}_2\right) &= U_2\rho_2 + K\sqrt{\rho_1\rho_2}e^{-i(\theta_2-\theta_1)}\end{aligned}\tag{B.3}$$

Now we define $\delta = \theta_2 - \theta_1$ and separate the equations into their real and imaginary

parts, giving us four equations:

$$\begin{aligned}
 \dot{\rho}_1 &= \frac{2}{\hbar} K \sin \delta \\
 \dot{\rho}_2 &= -\frac{2}{\hbar} K \sin \delta \\
 \dot{\theta}_1 &= -\frac{U_1}{\hbar} - \frac{K}{\hbar} \sqrt{\frac{\rho_2}{\rho_1}} \cos \delta \\
 \dot{\theta}_2 &= -\frac{U_2}{\hbar} - \frac{K}{\hbar} \sqrt{\frac{\rho_1}{\rho_2}} \cos \delta
 \end{aligned} \tag{B.4}$$

The current transported through the insulator is,

$$I = 2e\dot{\rho}_1 = -2e\dot{\rho}_2 = \frac{4e}{\hbar} K \sin \delta = I_c \sin \delta, \tag{B.5}$$

the factor 2 comes from that current is transported as Cooper-pairs, i.e. two electrons. The two last equations in (B.3) gives us how the phase changes with time,

$$\dot{\delta} = \dot{\theta}_2 - \dot{\theta}_1 = \frac{U_1 - U_2}{\hbar} + \frac{K}{\hbar} \left(\sqrt{\frac{\rho_2}{\rho_1}} - \sqrt{\frac{\rho_1}{\rho_2}} \right) \cos \delta. \tag{B.6}$$

If we assume $\rho_1 = \rho_2$ the phase derivative is proportional only to the energy difference between the two sides, which for example can be introduced by putting a voltage V over the junction, yielding $\dot{\delta} = \frac{eV}{\hbar}$. If we integrate this with respect to time, assume a constant voltage and plug it into equation (B.5) we get $I = I_c \sin(eVt/\hbar)$, i.e. we get oscillations in the current with angular frequency eV/\hbar

C

Derivation of the superconducting phase in two coupled resonators

Consider the system in figure C.1. We have the wave equation for the field inside a cavity

$$\ddot{\varphi} - \frac{1}{L_0 C_0} \varphi'' = 0, \quad (\text{C.1})$$

where L_0 and C_0 is the inductance and capacitance per unit length. We also have two boundary conditions from the SQUIDS

$$\frac{\hbar^2}{E_{CJ}} \ddot{\varphi}(d) + 2E_J \cos f_R \sin \varphi(d) + E_{L,cav} d\varphi'(d) = 0, \quad (\text{C.2})$$

$$\frac{\hbar^2}{E_{CJ}} \ddot{\varphi}(-d) + 2E_J \cos f_L \sin \varphi(-d) - E_{L,cav} d\varphi'(-d) = 0, \quad (\text{C.3})$$

where $E_{CJ} = (2e)^2/(2C_J)$, $E_J = (\hbar/2e)^2/L_J$ and $E_{L,cav} = (\hbar/2e)^2/(L_0 d)$. L_J is the inductance of one SQUID. Now add a capacitance C_c in the middle at $x = 0$

$$\frac{\hbar^2}{E_{C_c}} (\ddot{\varphi}(0+) - \ddot{\varphi}(0-)) + E_{L,cav} d\varphi'(0+) = 0, \quad (\text{C.4})$$

$$\frac{\hbar^2}{E_{C_c}} (\ddot{\varphi}(0-) - \ddot{\varphi}(0+)) - E_{L,cav} d\varphi'(0-) = 0, \quad (\text{C.5})$$

where $E_{C_c} = (2e)^2/(2C_c)$. Adding these two equations gives $\varphi'(0+) = \varphi'(0-)$, i.e. the derivative of the phase must be continuous. To calculate the cavity spectrum we linearize equations (C.2) and (C.3). This is possible since $\varphi(x)$ will be close to zero near the boundaries due to the fact that they are grounded there

$$2C_J \ddot{\varphi}(d) + \frac{2}{L_R} \varphi(d) + \frac{1}{L_0} \varphi'(d) = 0, \quad (\text{C.6})$$

$$2C_J \ddot{\varphi}(-d) + \frac{2}{L_R} \varphi(-d) - \frac{1}{L_0} \varphi'(-d) = 0, \quad (\text{C.7})$$

where $1/L_{R,L} = \cos f_{R/L}/L_J$ are the inverse Josephson inductances of the SQUIDS at respective side. We now make an ansatz for the solution

$$\varphi(\pm x, t) = e^{-i\omega t} (a_{\pm} \cos kx + b \sin kx) + c.c., \quad (\text{C.8})$$

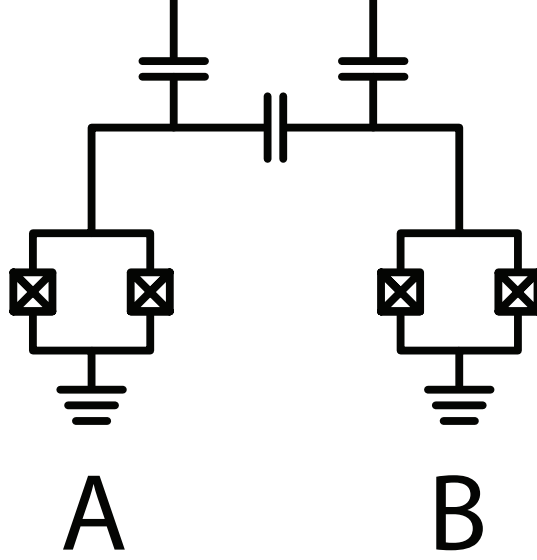


Figure C.1: Two coupled $\lambda/4$ resonators each terminated by a SQUID.

where $\omega = k/\sqrt{L_0 C_0}$. We insert the ansatz into equations (C.6), (C.7) and (C.4), it is enough to take only the first term of the ansatz

$$\left(\frac{2}{L_R} - 2C_J\omega^2\right)(a_+ \cos kd + b \sin kd) + \frac{k}{L_0}(-a_+ \sin kd + b \cos kd) = 0, \quad (\text{C.9})$$

$$\left(\frac{2}{L_L} - 2C_J\omega^2\right)(a_- \cos kd - b \sin kd) - \frac{k}{L_0}(a_- \sin kd + b \cos kd) = 0, \quad (\text{C.10})$$

$$a_+ - a_- = \frac{k}{2\omega^2 C_c L_0} b. \quad (\text{C.11})$$

Let us introduce $\tilde{a} = a_+ - kb/(4\omega^2 C_c L_0) = a_- + kb/(4\omega^2 C_c L_0)$ and rewrite equations (C.9) and (C.10) as

$$\begin{aligned} & \left[\left(\frac{2}{L_R} - 2C_J\omega^2\right) \cos kd - \frac{k}{L_0} \sin kd \right] \tilde{a}_+ \\ & \left[\left(\frac{k}{L_0} + \left(\frac{2}{L_R} - 2C_J\omega^2\right) \frac{k}{4\omega^2 C_c L_0}\right) \cos kd + \left(\frac{2}{L_R} - 2C_J\omega^2 - \frac{k^2}{4\omega^2 C_c L_0^2}\right) \sin kd \right] b = 0, \end{aligned} \quad (\text{C.12})$$

$$\begin{aligned} & \left[\left(\frac{2}{L_L} - 2C_J\omega^2\right) \cos kd - \frac{k}{L_0} \sin kd \right] \tilde{a}_- \\ & \left[\left(\frac{k}{L_0} + \left(\frac{2}{L_L} - 2C_J\omega^2\right) \frac{k}{4\omega^2 C_c L_0}\right) \cos kd + \left(\frac{2}{L_L} - 2C_J\omega^2 - \frac{k^2}{4\omega^2 C_c L_0^2}\right) \sin kd \right] b = 0. \end{aligned} \quad (\text{C.13})$$

Solving these equations can only be done numerically, where k is the unknown variable.